On Stratified Flow over a Ridge Intersecting Coastlines

ROXANA C. WAJSOWICZ*

Robert Hooke Institute, University of Oxford, Clarendon Laboratory, Oxford, United Kingdom

(Manuscript received 6 August 1990, in final form 31 December 1990)

ABSTRACT

The adjustment between two interconnecting basins of stratified fluid, resulting from the formation of a pool of dense water in one, is investigated with an 18-level numerical general circulation model (GCM). It is found that basic features of the adjustment, i.e., (i) the generation of low-frequency, coastally trapped Kelvin waves, which carry information about the alongshore pressure gradient, created by the denser water, toward the dividing ridge; (ii) the subsequent generation of barotropic double Kelvin waves by the JEBAR (Joint Effect of Baroclinicity and Relief) effect, which propagate infinitely rapidly along the ridge setting up an anticyclonic gyre; (iii) the generation of further coastally trapped Kelvin waves at the opposite coast due to an alongshore pressure gradient, created by upwelling at the ridge edge associated with the closure of the barotropic gyre; (iv) the generation of a coastally confined cyclonic gyre at the opposite ridge edge by the JEBAR effect and viscous and diffusive processes as the coastally trapped Kelvin waves cross off the ridge, are reproduced by an equivalent linear, f-plane, two-layer model with the topography confined to the lower layer. Features, which arise from the increased number of vertical degrees of freedom in the GCM, are found to include (i) a further sheltering of the upper levels from the presence of the ridge due to energy in the coastally trapped Kelvin waves being redistributed between various vertical modes; (ii) a baroclinic adjustment at the ridge face to eradicate any horizontal density gradients there, which takes the form of a Kelvin-type wave trapped against the face not previously described; and (iii) penetration of the circulation below the top of the ridge in the second basin due to vertical viscous and diffusive effects, as well as the dispersion of coastally trapped Kelvin waves of differing vertical modes.

First-order estimates of the magnitude of the baroclinic signals propagating on and away from the ridge are found by consideration of continuity of mass flux. Assuming that the fields may be decomposed into local vertical normal modes, a simple model with uniform stratification is used to derive analytic estimates of the relative amplitudes of the vertical modes, which compare favorably with those calculated from the GCM. Assuming that the energy of the coastally trapped Kelvin wave initially incident on the ridge is chiefly in the first baroclinic mode, then it is found that the higher the ridge, the less the energy scattered into the first-order mode propagating across the ridge (that in the higher-order modes remains small), and the greater the energy scattered into a first-order mode propagating along the face of the ridge and along the opposite coast. Also, a higher ridge results in more energy being scattered into higher-order mode, coastally trapped Kelvin waves propagating in the second basin. The magnitude of the barotropic response is found to be such as to cancel the vertical average of the baroclinic flow over the ridge face associated with the incident coastally trapped Kelvin waves for the anticyclonic gyre, and dependent on viscous and diffusive processes for the cyclonic gyre.

As well as ridges of top-hat cross section and differing heights, ridges with a pyramid cross section, i.e., "sloping" sides, and with an island (cf. Iceland) on top, are considered.

The implications of features of the adjustment for modeling the Atlantic thermohaline circulation and the transport of passive tracers are discussed, as these highlight aspects of the formulation of topography in GCMs, which merit further consideration in the general development of GCMs.

1. Introduction

Two fundamental questions arise from the study of the thermohaline circulation: How is the deep water formed in the polar regions and how does this water make its way into the midlatitude ocean basins? The latter question is nontrivial, since, for example, the Icelandic Ridge acts as a barrier to the flow of deep water formed in the Norwegian and Arctic seas into the North Atlantic. Attempts to model this circulation in a global context have been limited. Cox (private communication) indicated that the large-scale numerical climate general circulation models (GCMs) have difficulty in producing sufficient flux of deep water from polar regions to midlatitudes, thus affecting the poleward heat budget in the North Atlantic. The problem may be overcome to some extent by putting a boundary at 60°N, say, and relaxing the temperature and salinity fields there to climatology, but this is not a satisfactory solution in the long term development of GCMs. At

* Present Affiliation: The Institute of Low Temperature Science.

Corresponding author address: Dr. Roxana C. Wajsowicz, The Institute of Low Temperature Science, Hokkaido University, Sapporo, 060, Japan.

this stage, it would be useful to investigate further the interactions, which occur between a buoyancy-driven flow and a topographic barrier in the context of the physics and dynamics prescribed in a typical GCM.

A simple scenario is considered, which illustrates the mechanisms suggested by Gill (1977), that give rise to the differing background stratifications on either side of, say, the Icelandic Ridge system, i.e., a reservoir of fairly homogeneous water below the sill on the deep-water production side and stratified water on the other side with a tongue of deep water extending down the face of the sill to some depth. The study also illustrates various topographic interactions in a stratified fluid, which will occur due to a low-frequency (i.e., $\omega/f \ll 1$) coastally trapped density anomaly of large alongshore extent encountering a decrease and an increase in fluid depth, and also those due to a barotropic coastal jet encountering a decrease in fluid depth. These will have a general application throughout the world oceans. A simple rectangular basin of uniform depth filled with stratified fluid is divided into two basins by a ridge of arbitrary height, with width and length much larger than the internal Rossby radius; see Fig. 1. A pool of denser fluid is specified at time zero near the northern boundary, corresponding to production by a series of convective events. The initial adjustment will involve the generation of a coastally trapped Kelvin wave packet, which will propagate rapidly toward the ridge; see Hsieh and Gill (1986). The associated advection of a newly created water mass by a single event will be small. The adjustment in an equivalent shallow-water model may be deduced from Gill et al. (1986) and has been confirmed by numerical integration: the low-frequency perturbation propagates onto the ridge without change in amplitude at the coast, but with a phase speed and offshore decay-scale reduction by a factor $\gamma^{1/2}$, the ratio of the gravity wave speeds off-ridge to on-ridge. The implied reduction in mass flux is accounted for by a perturbation of the same height propagating out along the ridge; the form of this along-ridge adjustment for a top-hat ridge cross section is the double Kelvin wave, as described by Longuet-Higgins (1968). For low-frequency motions, the trapping-scale either side of the ridge edge is the respective Rossby radius and the phase speed is the difference in gravity wave speed off and on the ridge. At the opposite ridge edge, double Kelvin waves propagate into the coast, and a thin boundary layer, whose form depends on the parameterization of viscous and diffusive processes and inertial effects, develops at the intersection of the ridge edge with the coast. There is a reduction in height perturbation at the coast across the ridge edge of $\sim\gamma^{-1}$, consistent with a continuity in mass flux.

In a stratified fluid, double Kelvin waves have both a barotropic and a baroclinic component, which leads to a qualitatively different adjustment. This is described first for a two-layer model in section 2, where continuity of mass flux arguments are found to give good first-order estimates of the amplitude of the baroclinic signal propagating around the basin (cf. Gill et al. 1986). The differences in the adjustment process resulting from an increased number of vertical degrees of freedom are investigated in section 3. It is found useful to consider the motion in each basin as composed of vertical normal modes with horizontal and temporal structure governed by the shallow-water equations with differing baroclinic Rossby radii; cf. Wajsowicz and Gill (1986). On this basis, a simple model with uniform stratification is used to derive analytic estimates of the relative amplitudes of the vertical modes generated. The predicted variation with ridge height of energy scattered between the vertical modes is compared with results from an 18-level general circulation model in section 4. Ridges with top-hat cross sections and different heights are considered, as are ridges with more structure: a pyramid cross section evoking a slope, and an island (cf. Iceland) on top of the ridge. Discussion of the adjustment and how it suggests that the observed stratification across sills arise is given in section 5, along with a discussion of aspects of Bryan–Cox-type general circulation models, which the study has highlighted as needing further consideration and improvement.

2. A linear two-layer model with a rigid lid

a. Basic nondimensional equations

The basic geometry considered is illustrated in Fig. 1. In the simple models of the following sections, it is assumed that the Coriolis parameter f is constant, and that the variation in topography is independent of x. For ease of discussion, the positive y direction is taken as north. The two-layer equations may be written as separate prognostic equations for the baroclinic and barotropic modes by making the rigid-lid and Boussinesq approximations. The nondimensional linear equations of motion for the baroclinic response are

$$\hat{u}_t - \hat{v} = h_x + A_M\nabla^2\hat{u}, \quad (2.1a)$$

$$\hat{v}_t + \hat{u} = h_y + A_M\nabla^2\hat{v}, \quad (2.1b)$$

$$h_t + (D_2u_2)_x + (D_2v_2)_y = A_H\nabla^2h, \quad (2.1c)$$

where the variables have been nondimensionalized as follows

$$(x, y) \to \frac{c_0}{f}(x, y)$$

$$t \to \frac{1}{f}t$$

$$(u_1 - u_2, v_1 - v_2) = (\hat{u}, \hat{v}) \to c_0(\hat{u}, \hat{v})$$

$$h \to \frac{{c_0}^2}{g'}h.$$

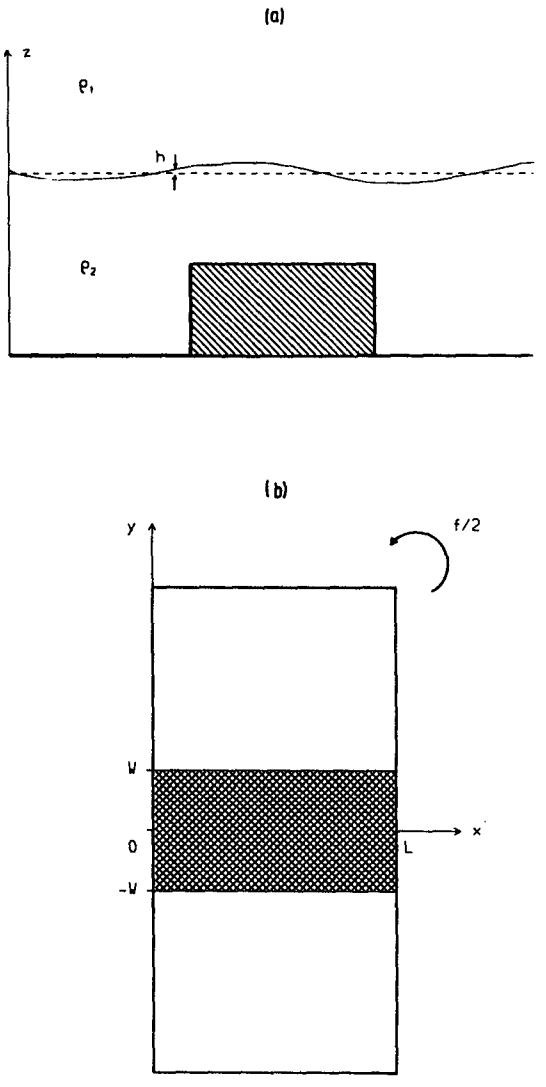

FIG. 1. Vertical section (a) and plan view (b) of the basic geometry.

The internal gravity wave speed c_0 is defined as

$$c_0^2 = g' \frac{H_1 H_{2O}}{H_1 + H_{2O}},$$

where g' is the reduced gravity $g(\rho_2 - \rho_1)/\rho_2$ and H_1 (H_{2O}) are the mean depths of the upper (lower) layers in the deep ocean. The layer depths H_1, H_2 are nondimensionalized on c_0^2/g' to give D_1, D_2. A lateral viscosity, which represents the transfer of momentum to unresolved scales, is incorporated in the form $A_M\nabla^2\mathbf{u}$, where A_M is a nondimensional constant coefficient. Lateral diffusion is incorporated in the form $A_H\nabla^2 h$, where A_H is a nondimensional constant coefficient. The barotropic response may be solved in terms of a streamfunction, ψ nondimensionalized on c_0^4/fg', defined by

$$\psi_x = D_1 v_1 + D_2 v_2,$$
$$-\psi_y = D_1 u_1 + D_2 u_2, \qquad (2.2)$$

which satisfies the nondimensional equation

$$\left\{\left(\frac{\psi_x}{D}\right)_x + \left(\frac{\psi_y}{D}\right)_y\right\}_t + \left(\frac{\psi_x}{D}\right)_y - \left(\frac{\psi_y}{D}\right)_x$$
$$= -\left(\frac{c^2}{D_1} h_y\right)_x + \left(\frac{c^2}{D_1} h_x\right)_y + A_M\left\{\left(\nabla^2 \frac{\psi_y}{D}\right)_y + \left(\nabla^2 \frac{\psi_x}{D}\right)_x\right\} + A_M\left\{\frac{1}{D}\nabla^2(c^2\hat{v}) - c^2\nabla^2\left(\frac{\hat{v}}{D}\right)\right\}_x$$
$$- A_M\left\{\frac{1}{D}\nabla^2(c^2\hat{u}) - c^2\nabla^2\left(\frac{\hat{u}}{D}\right)\right\}_y, \qquad (2.3)$$

where $c^2 = D_1 D_2/D$, $D = D_1 + D_2$. Equation (2.1c) may be rewritten in terms of the baroclinic velocities and ψ,

$$h_t - (c^2\hat{u})_x - (c^2\hat{v})_y = \left(\frac{c^2}{D_1}\psi_y\right)_x - \left(\frac{c^2}{D_1}\psi_x\right)_y + A_H\nabla^2 h. \qquad (2.1c')$$

Two nondimensional parameters will be used to describe the topography. These are $\Gamma = (1 + H_{2O}/H_1)/(1 + H_{2R}/H_1)$, the ratio of the total fluid depth of the deep ocean to that on the ridge, and $\gamma = \Gamma^{-1}H_{2O}/H_{2R}$, the square of the ratio of the internal gravity wave speed of the deep ocean to that on the ridge. The nondimensional upper-layer depth, $D_1 = (1 + H_1/H_{2O}) = (\Gamma - \gamma^{-1})/(\Gamma - 1)$, and the nondimensional lower-layer depths off and on the ridge are $D_{2O} = (1 + H_{2O}/H_1) = (\Gamma - \gamma^{-1})/(1 - \gamma^{-1})$ and $D_{2R} = D_{2O}/(\Gamma\gamma)$, respectively. For a two-layer model with a rigid lid, a reduced-gravity model is recovered in the limit as $H_1/H_2 \to \infty$, giving $\Gamma \to 1$ and $\gamma \to D_{2O}/D_{2R}$. Suppose $H_1 = 500$ m, $H_{2O} = 3500$ m, and $H_{2R} = 500$ m, then $\Gamma = 4$ and $\gamma = 1.75$; typically, if $H_1 \ll H_{2O}, H_{2R}$, then $\gamma \sim 1$ and $\Gamma \sim H_{2O}/H_{2R}$.

In the following numerical experiments, the above equations are integrated forward in time from initial conditions of rest and a uniform interfacial height perturbation in the northern third of the basin. The first stage of interest in the adjustment is the propagation of low-frequency, coastally trapped Kelvin waves toward the ridge, which impose the initial interfacial height perturbation along the west coast. Before presenting the numerical results, it is useful to consider first the dynamical processes that are expected to occur on the signal encountering the ridge.

b. *Analytic estimates of the magnitude of the response*

1) ADJUSTMENT AT NORTHERN RIDGE EDGE, ($y = W$)

A barotropic response is generated at the ridge edge through the JEBAR (Joint Effect of Baroclinicity and Relief) term, i.e., $-\{\hat{\mathbf{z}}\cdot\nabla\times(c^2/D_1)\nabla h\}$ in (2.3). For

a step discontinuity in depth, (2.3) reduces to $(\partial_t - A_M\nabla^2)\nabla^2\psi = 0$ on either side of the depth discontinuity with boundary conditions that $\psi = 0$ along the coast, and a no-slip (say) condition $\mathbf{n}\cdot(\hat{\mathbf{z}} \times \nabla\psi) = 0$ at the coast, where $\mathbf{n}$ is the unit vector normal to the coast. Matching conditions at $y = \pm W$ are obtained by integrating (2.3) across the depth discontinuity, yielding

$$\left[\frac{\psi_{yt}}{D} + \frac{\psi_x}{D}\right] = \left[\frac{c^2}{D_1} h_x\right] + A_M\left[\frac{\nabla^2\psi_y}{D}\right], \quad (2.4)$$

where [ ] denotes the jump in passing from $y = \pm W-$ to $y = \pm W+$. The condition (2.4) may be rewritten as $[\eta_x] = 0$, where η is the surface elevation.

In a two-layer ocean, the double Kelvin wave has both barotropic and baroclinic components; see, e.g., Rhines (1977). The properties of free waves in a two-layer ocean, as described by Eqs. (2.1)–(2.3), are outlined in the Appendix along with the modification for a ridge of finite width. Long waves, i.e., zonal wavenumber $m \ll 1$, are essentially barotropic and propagate infinitely fast for $m = 0$ as a result of the rigid-lid approximation. Hence, over the baroclinic western boundary layer and in the interior, it may be expected that the horizontal length scales for ψ will be $\geq O(1)$ at the northern ridge edge, and also from (2.1b) that h will be continuous across the edge. In this case, on time scales much greater than the inertial period and assuming $A_M^{1/2} \ll 1$, so that the time-dependent and viscous terms may be neglected, (2.4) gives an estimate for ψ_x, which is continuous across $y = W$ from conservation of total mass; namely,

$$\psi_x \approx -D_1 h_{Ox} \quad \text{at} \quad y = W, \quad \text{for} \quad 0 \leq x < L - \delta_E, \quad (2.5)$$

where δ_E is the width of the eastern boundary layer. Hence, since $\hat{v} \approx -h_{Ox}$ to first order,

$$v_2 \equiv \frac{\psi_x - D_1\hat{v}}{D} \approx 0 \text{ at } y = W, \text{ for } 0 \leq x < L - \delta_E.$$

In this case, there is negligible excess mass flux in the lower layer in the western boundary layer at the northern ridge edge, and so no need for a further slower adjustment in the form of two-layer double Kelvin waves with a significant baroclinic component propagating eastward from this region. Integrating (2.5) wrt x from the west coast ($x = 0$), where $\psi = 0$, gives that ψ increases across the baroclinic western boundary layer to a maximum of

$$\psi_I \approx D_1 h_O(x = 0)$$

and remains at this value across the interior, assuming $h_O \to 0$ in the interior. It will decrease to zero at the east coast over an infinitesimal singular region in which the time-dependent and viscous terms in (2.4) are no longer negligible.

Integrating (2.1c) across $y = W$ gives $[D_2 v_2] = A_H[h_y]$, and so it would appear that flow can be supported in the lower layer across the ridge edge by a diffusive flux. However, if this were nonzero, it would imply a discontinuity in flux in the upper layer, and hence that v_1 was discontinuous. Therefore, assuming $[D_2 v_2] = 0$,

$$\psi_x = \frac{D_1}{(1 - 1/\gamma)}\left(\hat{v}_O - \frac{1}{\gamma}\hat{v}_R\right), \quad (2.6a)$$

and

$$v_2(y = W+) = (\Gamma\gamma)^{-1} v_2(y = W-)$$
$$= \frac{1}{(\gamma\Gamma - 1)}(\hat{v}_O - \hat{v}_R), \quad (2.6b)$$

where $\hat{v}_O$, $\hat{v}_R$ are the values of $\hat{v}$ at $y = W+$, $W-$, respectively. If v_2 is continuous, then it is identically zero (and so $\hat{v}_O = \hat{v}_R$), giving $\psi_x = D_1\hat{v}$ at $y = W$, which agrees with (2.5), assuming $\hat{v} \approx -h_x$.

In an ideal continuum, the interfacial height field associated with the coastally trapped Kelvin wave packet would take the form $h = h_O(y + t)\, e^{-x}$ north of the ridge and $h = h_R(y + \gamma^{1/2}t)\, e^{-\gamma^{1/2}x}$ on the ridge. If h is continuous across the ridge edge, then there will have to be a boundary layer centered on the edge over which these two fields are matched. In a model with lateral viscosity and diffusion, the coastally trapped Kelvin-wave structure will have a more complex offshore exponential decay structure with boundary layers whose scales are dependent on the lateral viscosity and diffusion coefficients and the Rossby radius; see Davey et al. (1983). The respective h fields will be matched across the ridge edge through a viscous–diffusive boundary layer of width $O(A_M^{1/2}, A_H^{1/2})$.

2) Baroclinic response at east coast, ($x = L$)

The closure of the anticyclonic gyre in an eastern boundary layer will produce a divergence over the topography, and thus an interfacial height perturbation, which will propagate up the eastern boundary away from the ridge as a coastally trapped Kelvin wave packet. Integrating (2.1c′) over the width of the basin and between y_1 ($|y_1| \ll W - 1$) and y_2 ($\gg W + 1$) yields

$$\int_0^L \{\gamma^{-1}\hat{v}|_{y=y_1} - \hat{v}|_{y_2}\}\,dx = -\int_0^L \int_{y_1}^{y_2} h_t\,dy\,dx + A_H\int_0^L \{h_y|_{y_2} - h_y|_{y_1}\}\,dx, \quad (2.7)$$

where the boundary conditions ψ, $\hat{u}$, $h_x = 0$ at $x = 0$, L and matching conditions $[\psi_x]$, $[\hat{u}]$, $[h] = 0$, and $[D_2 v_2] = A_H[h_y]$ have been applied. If ω^2, $\gamma^{3/2}\omega A_M \ll 1$ ($\omega > 0$), then the coastally trapped Kelvin waves are approximately geostrophic in their alongshore di-

rection. Therefore, the lhs of the above reduces to $h_O - \gamma^{-1}h_R - h_E$, where h_O, h_E are the interfacial heights at $(x, y) = (0, y_2)$ and (L, y_2), respectively, and h_R that at $(0, y_1)$, where it is assumed that there is no baroclinic signal on the ridge at the east coast. If y_2 is well behind the front propagating up the east coast, and $\omega(y_2 - y_1) \ll 1$, $\omega A_H \ll 1$, then the terms on the rhs of (2.7) will be negligible and the above will reduce to

$$h_O - \gamma^{-1}h_R - h_E \approx 0.$$

Therefore, as the coastal amplitude of the signal propagating onto the ridge is unchanged to first order, i.e., $h_R \sim h_O$, the coastal amplitude of the signal propagating up the east coast, $h_E \sim (1 - \gamma^{-1})h_O$. If the rigid-lid approximation were not made, the fastest barotropic double Kelvin waves would cross the basin in a time $L/(1 - \Gamma^{-1/2})$, instead of instantly. Qualitatively, however, we would expect the adjustment to be similar.

3) ADJUSTMENT AT SOUTHERN RIDGE EDGE, ($y = -W$)

At this step, double Kelvin waves propagate into the west coast. Therefore, it may be expected that the horizontal scales will be $\geq O(1)$ outside a narrow, western boundary layer of width δ_W. Applying (2.4) across $y = -W$ and integrating wrt x from the east coast ($x = L$) to δ_W (cf. 2.5, where now $h \approx 0$, $\delta_W < x \leq L$) gives, for time scales much greater than the inertial period and $A_M{}^{1/2} \ll 1$,

$$\psi \approx 0 \quad \text{at} \quad y = -W, \quad \delta_W < x \leq L.$$

Neglecting viscous effects, in the infinitesimal singular boundary layer, cf. Johnson (1985), from (2.4) to first order

$$\psi \approx -\frac{D_1}{(1 - 1/\gamma)}\left(h_T - \frac{1}{\gamma}h_S\right) \quad \text{at} \quad y = -W, \quad 0 \leq x < \delta_W \quad (2.8)$$

where h_S, h_T are the values of h at $y = -W+$, $-W-$, respectively, and where the x integration has been carried out from the interior toward the coast, i.e., the direction of propagation of the double Kelvin waves. If h were continuous across $y = -W$, then (2.8) would imply that ψ would become negative, and the boundary condition $\psi = 0$ at the coast could not be satisfied. If viscous effects are included, then there will be a narrow boundary layer at the coast through which h will be reduced by $\sim\gamma^{-1}$ and ψ brought to zero. This would imply the formation of a cyclonic gyre, though the actual structure will depend on the formulation of viscous and diffusive processes, and inertial effects if these are included.

Applying the equivalent of (2.7), where now $y_1 \ll -W - 1$ and $|y_2| \ll W - 1$, yields

$$h_T \approx \frac{1}{\gamma}h_S,$$

which is in agreement with the above.

For a ridge with a piecewise continuous cross-sectional profile, the setting up of the barotropic circulation on the ridge slopes will be via topographic Rossby waves, which can propagate in either direction, thus leading to a possibly more complex boundary-layer structure on the ridge. However, in the western boundary layer, one would expect the dominant balance in the barotropic vorticity equation (2.3) to be $\psi_x \approx -D_1 h_x$ for y such that $D_{2y} > 0$, giving $v_2 \approx 0$. Hence, once again, there would be no significant baroclinic adjustment propagating eastward along the slope, and no reduction in h at the coast onto the northern slope. In the eastern boundary layer, the dominant balance in the barotropic vorticity equation, initially, is $\psi_{xt} \sim (D_{2y}/D)\psi$, i.e., short topographic Rossby waves with the x scale decreasing with time. The balance is modified by lateral viscosity, yielding a steady Munk-type boundary layer with offshore decay scale of $(|D_{2y}|/A_M D)^{1/3}$. The return barotropic flow will generate a divergence such that initially on the slope

$$h_t \approx -\frac{D_1 D_{2y}}{D^2}\psi_x.$$

On the southern slope of the ridge ($D_{2y} < 0$), ψ will be zero outside a western boundary layer, in which positive vorticity is generated by the JEBAR terms and redistributed by short topographic Rossby waves. Approximate expressions for ψ on both slopes in the presence of lateral viscosity assuming a fixed exponentially decaying offshore structure for h were derived by Anderson and Corry (1985). Once again, estimates may be derived for the coastal amplitudes of the baroclinic signals propagating away from the ridge, as from (2.7), where now γ is replaced by its maximum (at $D_{2y} = 0$).

c. *Numerical solutions of the initial value problem*

A numerical model based on Eqs. (2.1)–(2.3) was started from rest with a uniform interfacial height perturbation, initiated over the first 6 hours, in the northern third of the basin. The model was formulated on a B grid and the bottom depth was treated in a similar way to that in the GCM used in section 4; see Cox (1984). The grid resolution was 1° of latitude, as in the GCM. Layer depths of $H_1 = 1000$ m and $H_2 = 2750$ m were chosen, giving the same total depth and level of change in sign in first baroclinic mode velocity as in the GCM. The reduced gravity is $0.001g$, thus, giving an internal gravity wave speed of 2.68 m s^{-1}, approximately the same as for the first baroclinic mode in the GCM. Results from models with ridge heights of 1200

and 2200 m are considered, which give parameter values of $\Gamma = 1.47$, $\gamma = 1.21$, and $\Gamma = 2.42$, $\gamma = 2.07$, respectively. The dimensional lateral diffusion coefficient, A_H^* is 5×10^3 m^2 s^{-1}, and so $A_H = 0.051$. The dimensional lateral viscosity coefficient, A_M^* is 5×10^4 m^2 s^{-1}, and so $A_M = 0.506$ in the first model, and double this in the second in order to maintain a well-resolved boundary layer at the northeast ridge edge.

The fields in the two models are shown in Fig. 2 at 60 days, which is sufficient time for the coastally

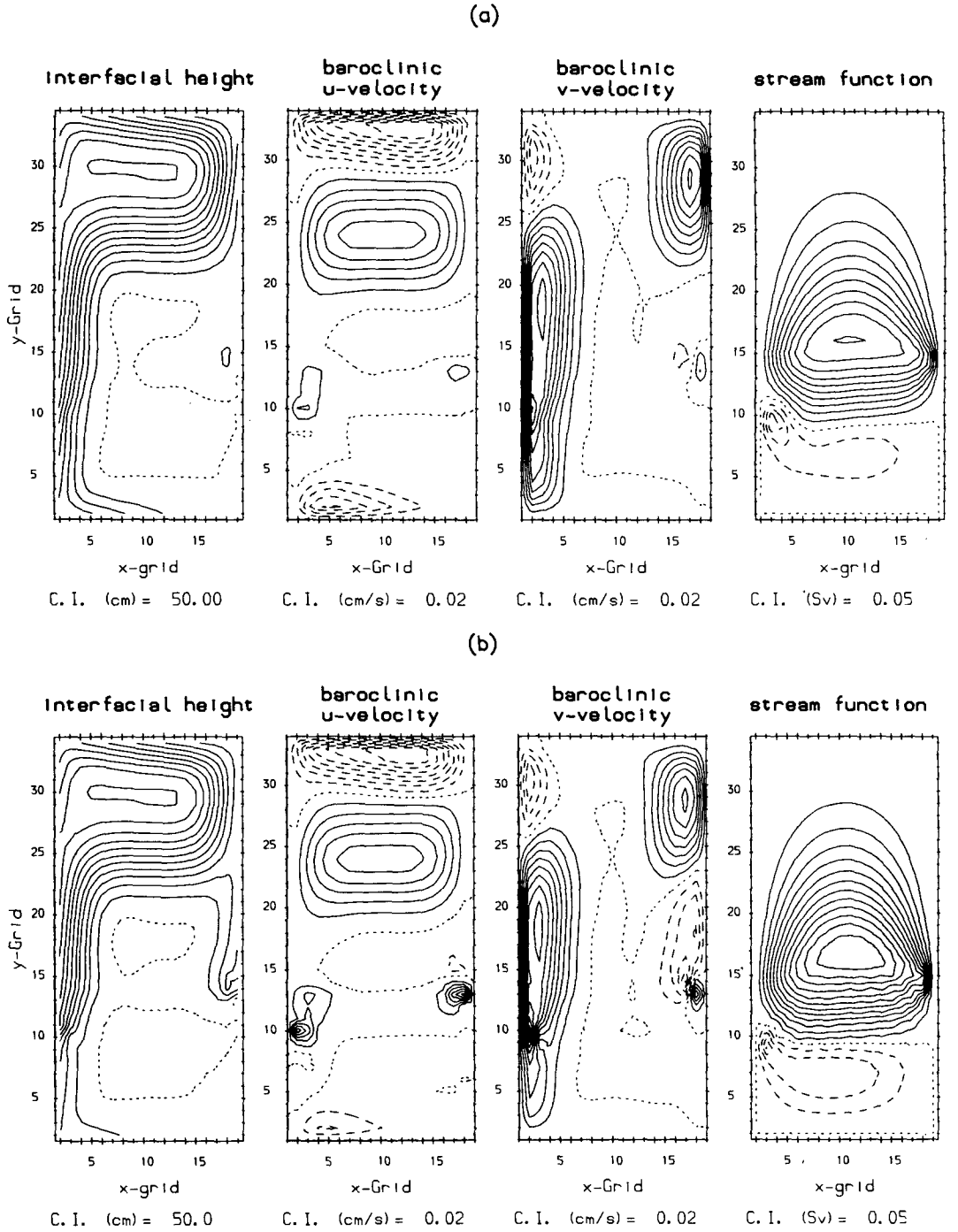

FIG. 2. The prognostic fields for a two-layer model with a rigid lid are shown at 60 days for (a) $\Gamma = 1.47$, $\gamma = 1.21$, and (b) $\Gamma = 2.42$, $\gamma = 2.07$. The ridge has a top-hat cross section, with the edges at $y_j = 10$ and $y_j = 15$. In this and subsequent figures, solid (dashed) contours denote positive (negative) values. The zero contour is denoted by a dotted line.

trapped signal to have crossed the ridge. The larger lateral viscosity coefficient is apparent in the higher ridge case through the increased boundary-layer width at the west coast. As expected from section 2b, an anticyclonic barotropic gyre, centered on the northern ridge edge extending across the width of the basin has formed. Its western boundary-layer width matches that of the baroclinic boundary layer, and the width at the east coast has thinned to a gridpoint width. From (2.5), ψ increases to a dimensional value of $(g'H_1/f) \times$ value of the interfacial height perturbation at the west coast. Taking this latter value as 4 m and $f = 7.27 \times 10^{-5}$ s^{-1}, this gives a maximum ψ as 0.54 Sv (Sv $\equiv 10^6$ $m^3 s^{-1}$), which is in good agreement with Fig. 2, where in both models $\psi_{max} \sim 0.5$ Sv at the ridge edge. Although, A_M is O(1) in the numerical model, the viscous terms in (2.4) are still an order of magnitude smaller than the JEBAR terms, as the y scale of ψ away from the eastern boundary is $O(W) \gg 1$. The temporal development of the barotropic streamfunction along the northern ridge edge is shown in Fig. 3a for the model depicted in Fig. 2a. The basinwide extent is instant, as expected for a rigid-lid model. There is some indication of propagation into the interior from the western boundary. However, the gradient of the line separating temporally increasing from uniform behavior is similar in both models and is found to be due to the increase in magnitude and broadening of the baroclinic meridional velocity field, which the barotropic flow adjusts to cancel in the lower layer. The time development of the corresponding lower-layer velocity along the west coast is shown in Fig. 3b. The rapid decrease in the vicinity of the northern ridge edge corresponding to the setting up of the compensating barotropic circulation is evident. When the Kelvin wave front initially encounters the ridge, the lower-layer velocity is the same on either side of the ridge edge for a couple of days. It then decreases on the deeper side of the ridge, such that by 90 days, it is only ~3% of the velocity on the higher edge.

There is flow onto the ridge in the lower layer through a viscous eastern boundary layer of width

$$\sim \left\{ \frac{1}{2} \left(\frac{\Gamma + 1}{\Gamma - 1} \right) A_M \Delta y \right\}^{1/3},$$

which for $\Gamma = 1.47$, $\Delta y = 3.0$, and $A_M = 0.5$ is 1.58 Rossby radii, or just over half a grid spacing and so just resolved by the model (hence the jaggered contours in Fig. 3a). The return southward barotropic flow generates baroclinicity at the east coast ridge edge, which may be seen in Fig. 2. In section 2b, it was predicted that the interfacial height perturbation should be about $(1 - \gamma^{-1})$ that at the west coast, i.e., ~0.17 for $\gamma = 1.21$, and ~0.52 for $\gamma = 2.07$, which is about 25% greater than observed in Fig. 2. Although h is quite steady at this stage at the west coast, it is still increasing along the east coast. The subsequent propagation up the east coast is more readily seen in Fig. 2b.

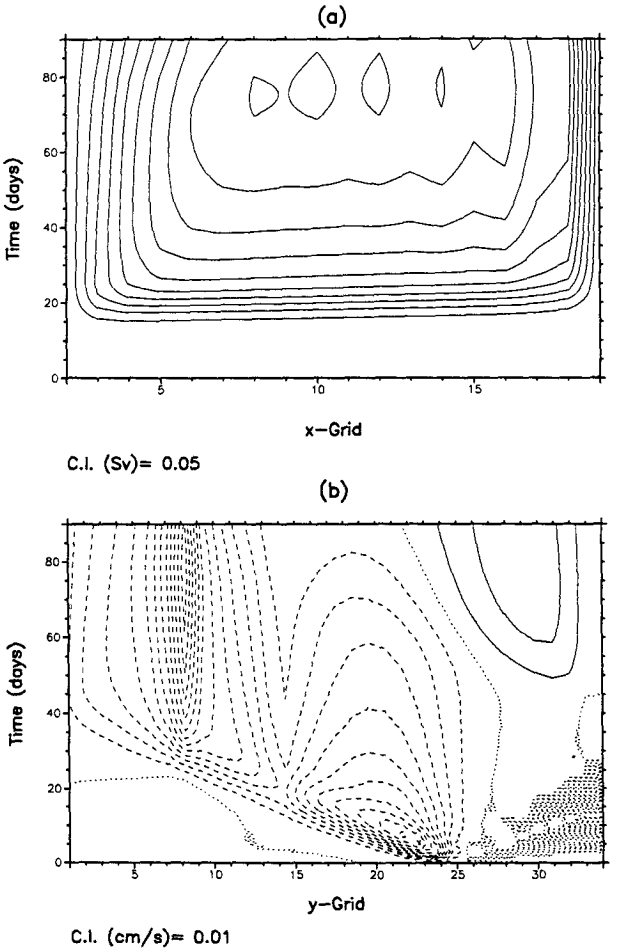

FIG. 3. The time variation of the barotropic streamfunction along the northern ridge edge is shown in (a), and that of the lower-layer meridional velocity field along the west coast is shown in (b), both for the model with $\Gamma = 1.47$, $\gamma = 1.21$.

At the southern ridge edge, a cyclonic gyre forms by the west coast; see Fig. 2. Its strength is only 40% that of the anticyclonic gyre in the model with $\Gamma = 1.47$ and half that in the model with $\Gamma = 2.42$. The center is a grid point away from the west coast, as expected from Johnson (1985). In between the gyre center and the west coast, where $\psi_x < 0$, the divergence term in (2.1c′), i.e., $-(c^2/D_1)_y \psi_x$ is negative, and so acts to reduce h with time. As x increases, ψ increases from its minimum over several grid points to zero and remains at this value across the basin, and so h is much less affected, as may be seen in Fig. 2. The variation of interfacial height with time along the west coast is shown in Fig. 4 for the two models. The formation of the front in h at the southern ridge edge corresponds to the increase in v_2, as shown in Fig. 3b. In section 2b, it was predicted that the coastal amplitude of h south of the ridge should be $\sim 1/\gamma \times$ the amplitude of h on the ridge, i.e., $\sim 0.82 h_S$ for $\gamma = 1.21$ and

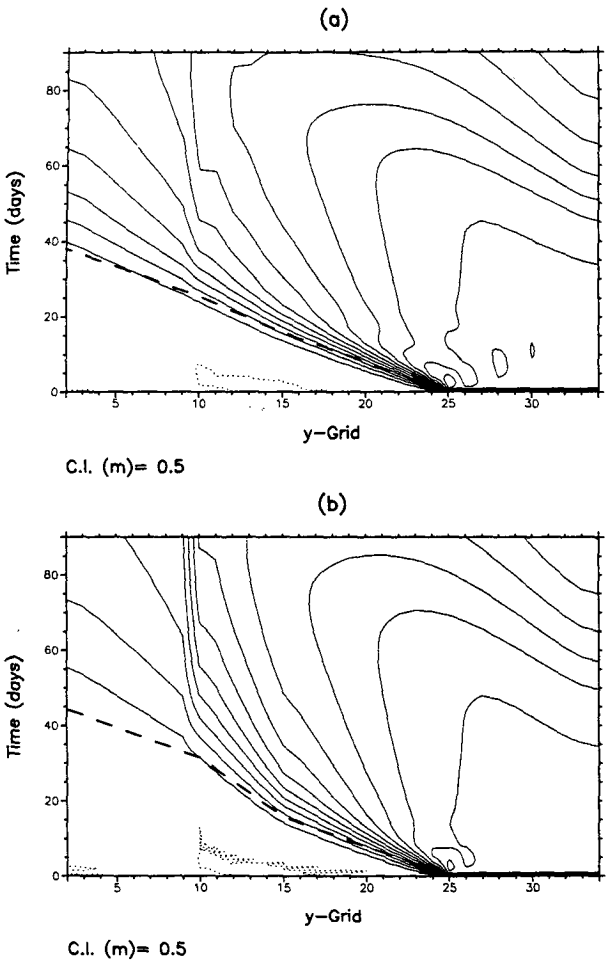

FIG. 4. The time variation of the interfacial height field along the west coast for the models with (a) $\Gamma = 1.47$, $\gamma = 1.21$, and (b) $\Gamma = 2.42$, $\gamma = 2.07$. The bold dashed line denotes the path as calculated using the theoretical nondispersive, resolution-dependent phase speeds for coastally trapped Kelvin waves derived from Hsieh et al. (1983).

$\sim 0.48 h_S$ for $\gamma = 2.07$. From Fig. 4, the values are ~ 0.8 and ~ 0.4, respectively.

The net upper- and lower-layer velocities associated with the fields shown in Fig. 2a are shown in Fig. 5. The effectiveness of stratification, as a result of the JEBAR effect, in sheltering the upper-layer flow and interfacial height perturbation from the underlying changes in topography is most apparent at the northwestern ridge edge. It occurs to some extent at the southwestern ridge edge as the northward barotropic flow almost cancels the southward baroclinic flow in the outer part of the boundary layer. The net flow is an intense coastal jet off the ridge in the lower layer, which is much narrower than the overlying northward flow. There is also a contrast in width of the net flow in the upper and lower layers at the northwest ridge edge. In addition to coastally trapped Kelvin waves being generated at $y = W+$, which take a positive coastal interfacial height northward, coastally trapped Kelvin waves will also be generated at $y = W-$, which try to reimpose a zero coastal interfacial height, and so give rise to a northward baroclinic flow next to the coast just at the ridge edge. For the $\Gamma = 2.42$ model, the fields are similar, though the induced baroclinic flow at the east coast is sufficiently large that well north of the ridge, where the barotropic flow is weak, the lower layer flow is northward.

The transport of passive tracers across a ridge by such a buoyancy-driven flow was investigated using a model in which the interfacial height at the northern boundary was held fixed at some positive value. The

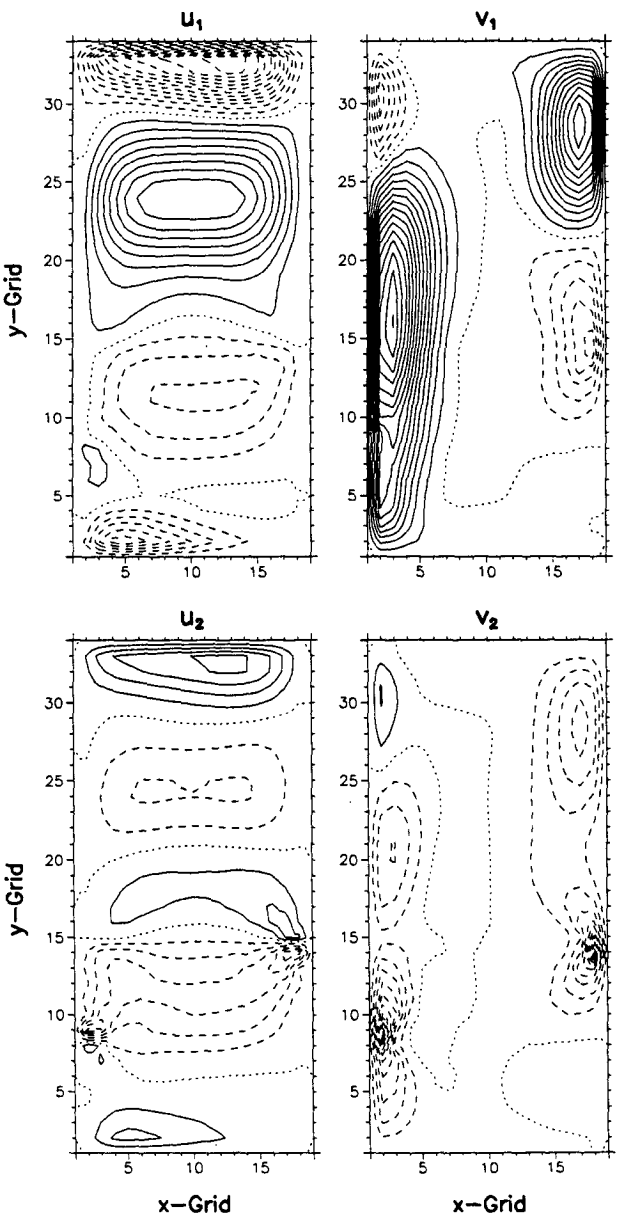

FIG. 5. The upper- and lower-layer velocity fields at 60 days for the model with $\Gamma = 1.47$, $\gamma = 1.21$.

resulting velocity field was very similar to that shown in Fig. 5 for the first couple of years. In the lower layer of the two-layer model, tracers are transported onto the ridge only through the Munk-type eastern boundary layer and not along the length of the ridge as in a shallow-water model. The baroclinic velocity generated at the eastern boundary is northward in the lower layer, and so only particles close to the ridge, where the southward barotropic flow is strongest, will be swept onto the ridge. These particles may have originated in the western boundary layer and have been advected across the basin by the weak zonal barotropic flow. Once on the ridge, the particles are swept westward by the barotropic flow and rapidly cross off the ridge through the narrow western boundary layer. There is still some question about whether the transport of deep water through the Denmark Strait, for example, is a transient phenomenon, occurring in surges, or a steady flow; see, e.g., Livingstone et al. (1985). The above results would tend to suggest that some care may be needed in the plotting of transient-tracer transport across sills, in that the tracers may not originate from the most obvious source and are likely to have taken a much longer path than may be supposed.

Experiments with smoother ridge cross sections were also carried out. The results were qualitatively similar, and quantitatively as predicted at the end of section 2b. The cross-sectional profile and height of the ridge determine the amplitude and speed of various stages of the adjustment, but not the actual form.

3. Extension to continuous stratification

In the next section, an 18-level general circulation model (GCM) is used to investigate the effect of an increased number of vertical degrees of freedom. First, though, aspects of the adjustment for a continuously stratified model, linearized about a background state of rest and background density $\rho_B(z)$ will be discussed.

a. Basic nondimensional equations

The equations governing the motion are

$$u_t - v = -p_x + A_M\nabla^2 u + \kappa_M u_{zz}, \quad (3.1a)$$

$$v_t + u = -p_y + A_M\nabla^2 v + \kappa_M v_{zz}, \quad (3.1b)$$

$$p_z = -\rho, \quad (3.1c)$$

$$u_x + v_y + w_z = 0, \quad (3.1d)$$

$$\rho_t + \rho_{Bz} w = A_H\nabla^2\rho + \kappa_H\rho_{zz}, \quad (3.1e)$$

where u, v are the total velocity perturbations, i.e., baroclinic plus barotropic components, and p, ρ are the pressure, density perturbations. The nondimensionalization is defined similarly to that for the two-layer model; namely,

$$(x, y) \to a_O(x, y)$$
$$z \to (c_O^2/g)z$$
$$\rho \to \rho_o\rho$$
$$p \to (c_O^2\rho_o)p$$
$$(u, v) \to c_O(u, v)$$
$$w \to (c_O^2 f/g)w$$

where $a_O(=c_O/f)$ is the first baroclinic mode Rossby radius, and ρ_o is a typical density. The Boussinesq approximation has been made, and the fluid is assumed to be in hydrostatic balance. Vertical viscosity with nondimensional coefficient κ_M has been included. Changes in density are assumed due to either vertical advection of the background density field or lateral and vertical diffusion. The nondimensional coefficient of vertical diffusion is κ_H. Integrating (3.1d) over the depth of the ocean and applying the rigid-lid condition $w = 0$ at $z = 0$ and the boundary condition of no normal flow at the bottom, i.e., $w = -uD_x - vD_y$ at $z = -D$, yields

$$\left\{\int_{-D}^{0} u dz\right\}_x + \left\{\int_{-D}^{0} v dz\right\}_y = 0. \quad (3.2)$$

Therefore, a ψ exists such that

$$\psi_x = \int_{-D}^{0} v dz, \quad \psi_y = -\int_{-D}^{0} u dz. \quad (3.3)$$

The barotropic vorticity equation, which is a prognostic equation for ψ, may be obtained by subtracting $[D^{-1} \times \int_{-D}^{0}(3.1a)dz]_y$ from $[D^{-1}\int_{-D}^{0}(3.1b)dz]_x$ and using the hydrostatic equation to replace p by an integral of ρ, giving

$$\left\{\left(\frac{\psi_x}{D}\right)_x + \left(\frac{\psi_y}{D}\right)_y\right\}_t + \left(\frac{\psi_x}{D}\right)_y - \left(\frac{\psi_y}{D}\right)_x = \left\{\frac{1}{D}\int_{-D}^{0}\int_{z}^{z_r}\rho_x dz'dz\right\}_y - \left\{\frac{1}{D}\int_{-D}^{0}\int_{z}^{z_r}\rho_y dz'dz\right\}_x + A_M\left\{\frac{1}{D}\int_{-D}^{0}\nabla^2 v dz\right\}_x - A_M\left\{\frac{1}{D}\int_{-D}^{0}\nabla^2 u dz\right\}_y, \quad (3.4)$$

where z_r is a reference level above the top of the ridge. For a step topography, the parameter Γ has the same definition as in the two-layer model, but now γ is replaced by γ_n, $n = 1, 2, 3, \cdots$, i.e., the ratio of the inverse square of the nth-mode gravity wave speed on the ridge to the nth-mode wave speed in the open ocean. A numerical method of solution for the above

set of equations may be found in Cox (1984), for example. Details of the solution will depend on the boundary conditions applied. In the GCM discussed in section 4, in which the topography is represented by stacked boxes, no-slip conditions are applied at vertical boundaries, and no normal flow and no tangential stress at horizontal ones. Also, a condition of no normal heat flux is applied at all boundaries.

b. *Analytic estimates of the magnitude of the response*

For simplicity, the resultant interactions when a first baroclinic mode coastally trapped Kelvin wave packet encounters a ridge will be considered. Once again, it is assumed that the frequency is much less than the inertial frequency, so that energy is scattered into coastally trapped Kelvin waves and double Kelvin waves only. It is also assumed that $U/(W|f|) \ll 1$, where U is a typical meridional velocity, so that the flow is in the quasi-geostrophic regime in the sense that perturbations generated will be trapped over the topography and not propagate vertically; e.g., see Gill (1982, §8.7 and 8.8v).

In the absence of viscous and diffusive effects or lateral advection, the ridge edges, $z = -D_R$, $y = \pm W$, would be lines of discontinuity for variables such as v and ρ. In the following discussion, it will be assumed that viscous and diffusive boundary layers form at these edges giving continuity of the various fields, but that these boundary layers with widths of order $l_H^{-1} \sim O(A_M^{1/2}, A_H^{1/2})$, $l_V^{-1} \sim O(\kappa_M^{1/2}, \kappa_H^{1/2})$ in the horizontal and vertical directions, respectively, are such that $l_H^{-1} \ll W$ and $l_V^{-1} \ll D_R$.

1) ADJUSTMENT AT THE NORTHERN RIDGE EDGE ($y = W$)

The passage of the coastally trapped Kelvin wave packet onto the ridge generates vorticity through the JEBAR terms in (3.4) such that

$$\left[\frac{\psi_{yt}}{D} + \frac{\psi_x}{D}\right] = \left[\frac{1}{D}\int_{-D}^{0}\int_{z}^{z_r} \rho_x dz'dz\right] + A_M\left[\frac{\nabla^2\psi_y}{D}\right] \quad (3.5)$$

where [ ] denotes the jump in a quantity in passing from $y = W-$ to $W+$, and ψ satisfies $(\partial_t - A_M\nabla^2)\nabla^2\psi = 0$ on either side. Equation (3.5) may be rewritten as $[p_x(z = z_r)] = 0$.

As in the two-layer model, a response will be set up infinitely fast along the length of the northern ridge edge by essentially barotropic double Kelvin waves. A further baroclinic adjustment is needed to satisfy the no-normal flow boundary condition at the ridge face. From the numerical model described in the next section, the barotropic adjustment is such as to cancel the depth-averaged flow over the depth of the ridge, and further adjustment takes the form of a Kelvin-type wave, which is confined to the depth of the ridge ($w = 0$ at $z = -D_O$ and $-D_R$) and is trapped against the northern face. It propagates eastward at a wave speed determined by the stratification over the depth of the ridge. This adjustment results in the density perturbation incident at $x = 0$, $y = W+$, $-D_R > z \geqslant -D_O$ being transmitted along the ridge face. This latter type of wave is quite different from the bottom-trapped baroclinic mode, with horizontal scale much less than the Rossby radius, described by Rhines (1977) for infinitesimal topography in a quasi-geostrophic system. Nor is it of the form considered by Chapman (1982) in his study of the structure of double Kelvin waves in a uniformly stratified fluid with a finite-height step, which was valid for $\omega \ll 1$, since its velocity is continuous at $z = -D_R$ only through vertical viscous effects not taken into account by Chapman.

Assuming length scales are $\geqslant O(1)$ over the western boundary layer and interior, (3.1b) gives that the total pressure is continuous across $y = W$. Also from (3.2), $[\psi_x] = 0$. Hence, on time scales greater than the inertial period, assuming $A_M^{1/2} \ll 1$, (3.5) gives an estimate for $\psi_x(y = W)$ of

$$(\psi_x)_N \approx \frac{1}{(1-\Gamma^{-1})}\left\{\int_{-D_R}^{0}\int_{z}^{z_r} \rho_{Rx}dz'dz - \Gamma^{-1}\int_{-D_O}^{0}\int_{z}^{z_R} \rho_{Nx}dz'dz\right\}$$

$$= \frac{D_O}{(\Gamma-1)}\{\hat{p}_R(z_r) - \hat{p}_N(z_r)\}$$

$$\text{for} \quad 0 \leqslant x < L - \delta_E \quad (3.6a)$$

where ρ_N, ρ_R are the density perturbations and $\hat{p}_N$, $\hat{p}_R$ are the baroclinic pressure peturbations, i.e., $p - D^{-1}\int_{-D}^{0} p dz$, at $y = W+$, $W-$, respectively, and δ_E is the width of the eastern boundary layer. In the absence of lateral advection and horizontal diffusion, the boundary condition $w = 0$ at $z = -D_R$ for $|y| < W$ would imply that no density perturbation could be supported at that level on the ridge. In the presence of weak diffusion, assuming $[\rho_x] = 0$, $0 \geqslant z > -D_R$, (3.6a) reduces to

$$(\psi_x)_N \approx \frac{1}{(1-\Gamma^{-1})}\int_{-D_R}^{0} \hat{p}_{Nx}dz$$

$$\text{at} \quad y = W, \quad \text{for} \quad 0 \leqslant x < L - \delta_E, \quad (3.6b)$$

which can be estimated by supposing $\hat{p}_N \sim \hat{p}_O$ for $0 \geqslant z > -D_R$.

From the continuity equation (3.1d), assuming w_z is finite across $y = W$ away from the eastern boundary layer, then v is continuous across $y = W$. Therefore,

$$\hat{v}_N + \frac{(\psi_x)_N}{D_O} = \hat{v}_R + \frac{(\psi_x)_N}{D_R}$$

$$0 \geqslant x > \delta_E, \quad 0 \geqslant z > -D_R \quad (3.7)$$

where $\hat{v}_N$, $\hat{v}_R$ are the baroclinic velocities at $y = W+$, $W-$, respectively. Integrating (3.7) from $z = 0$ to $-D_R$ gives

$$(\psi_x)_N = \frac{1}{(1 - \Gamma^{-1})} \int_{-D_R}^{0} \hat{v}_N dz, \qquad (3.8)$$

which is consistent with (3.6), assuming geostrophic balance and noting the topography does not vary with x, so that $\hat{p}_x = p_x - D^{-1} \int_{-D}^{0} p_x dz$. Substituting back in (3.7), gives $\hat{v}_R$. It is noteworthy that under these assumptions the baroclinic velocity field is discontinuous across $y = W$, unlike the two-layer model in which it was continuous. However, $\hat{v}_z$ will be continuous for $0 \geq z > -D_R$, so no discontinuity in ρ or its horizontal gradients is implied for $0 \geq z > -D_R$. From (3.8), assuming the average of $\hat{v}_N$ over the depth above the top of the ridge is positive, (which it will be for a cold anomaly with a first baroclinic mode structure), then ψ_x is positive, and an anticyclonic gyre will be generated at the northern ridge edge. From the boundary condition of no normal flow at the ridge face, the residual baroclinic flow, which will generate a Kelvin-type wave along the ridge face, is

$$\hat{v}_D = -\hat{v}_O - \frac{(\psi_x)_N}{D_O} \text{ at } y = W+, \ -D_R > z \geq -D_O. \qquad (3.9)$$

2) BAROCLINIC RESPONSE AT AN EAST COAST ($x = L$)

Initially, the vertical velocity field will have the form of a delta function, $w_z = \delta(y - W) \cdot (\Gamma - 1)\psi_x / D_O$, since ψ_x is continuous across $y = W$. However, this will generate a density perturbation, through (3.1e), which will propagate up the east coast as a coastally trapped Kelvin wave packet. If it is assumed that after some mutual adjustment between the baroclinic and barotropic fields, that v is continuous across $y = W$, then an estimate of the baroclinic meridional velocity at $y = W+$, $\hat{v}_E$ is given by

$$\hat{v}_E = (\Gamma - 1) \frac{(\psi_x)_E}{D_O}, \qquad 0 \geq z > -D_R, \quad 0 \leq L - x < \delta_E, \quad (3.10a)$$

where it has also been assumed that $\hat{v}(y = W-) = 0$, $0 \leq L - x < \delta_E$. From the no-normal flow boundary condition

$$\hat{v}_E = -\frac{(\psi_x)_E}{D_O}, \ -D_R > z \geq -D_O, \ 0 \leq L - x < \delta_E. \qquad (3.10b)$$

There will be a viscous–diffusive boundary layer centered at $z = -D_R$ across which the values of $\hat{v}_E$ are matched. From the thermal wind relationship, the above implies that $\rho_x (y = W+)$ will be very large in the neighborhood of $z = -D_R$, and hence from (3.1e), there will be a large upwelling at $z = -D_R$. Further details of the mutual adjustment will be described with the help of the GCM in the next section.

3) ADJUSTMENT AT SOUTHERN RIDGE EDGE ($y = -W$)

At the southern ridge edge, $y = -W$, in the time before the coastally trapped signal propagates around the southern boundary back to the ridge, there is no perturbation outside a western boundary layer, since the double Kelvin wave propagates westward at this edge. Integrating (3.5) from the interior into the western boundary layer yields

$$\psi \approx \frac{D_O}{(\Gamma - 1)} \{\hat{p}_S(z_r) - \hat{p}_T(z_r)\} \qquad \text{at } y = -W, \quad 0 < x < \delta_W \quad (3.11a)$$

on time scales much greater than the inertial period, assuming viscous effects are negligible, where $\hat{p}_S$, $\hat{p}_T$ are the baroclinic-pressure perturbations at $y = -W+$, $-W-$, respectively. The boundary condition $\psi = 0$ at $x = 0$ is satisfied if

$$\hat{p}_S(x = 0, z = z_r) = \hat{p}_T(x = 0, z = z_r). \qquad (3.11b)$$

From the continuity equation (3.1d), the total meridional velocity is continuous across $y = -W$, assuming w_z is finite, hence

$$\hat{v}_T + \frac{\psi_x}{D_O} = \hat{v}_S + \frac{\psi_x}{D_R} \quad 0 \geq z > -D_R \qquad (3.12a)$$

where $\hat{v}_S$, $\hat{v}_T$ are the baroclinic velocities at $y = -W+$, $-W-$, respectively. The boundary condition of no-normal flow at the ridge face gives

$$\hat{v}_T + \frac{\psi_x}{D_O} = 0, \quad -D_R > z \geq -D_O, \qquad (3.12b)$$

where $\hat{v}_T$ will be matched across $z = -D_R$ through a narrow viscous–diffusive boundary layer. Integrating (3.12) over the western boundary layer, $0 \leq x < \delta_W$, assuming the meridional baroclinic velocity is geostrophic to first order, gives

$$\hat{p}_T(x = 0) \approx \begin{cases} \hat{p}_S(x = 0), & 0 \geq z > -D_R \\ 0, & -D_R > z \geq -D_O, \end{cases}$$

in agreement with (3.11b). Following the two-layer model, if the adjustment off the ridge is such that the density perturbation is continuous across $y = -W$, then from the thermal wind balance, $v_{Sz} \approx v_{Tz}$ at $z = -D_R$. Hence, since $v_T \equiv 0$ at $z = -D_r-$ and $v_{Rz} \equiv 0$ at $z = -D_R$ from the boundary conditions, $v_S(-D_R) = 0$, and so $\psi_x \approx -D_R \hat{v}_S(-D_R)$ over the western boundary layer. This latter condition cannot hold throughout the layer if the boundary condition $\psi(x = 0) = 0$ is to be satisfied. Therefore, there must be a region next to the coast in which there is a large vertical shear in velocity

across $z = -D_R$. Downwelling will generate the required negative density perturbation, assuming $v_z < 0$. The magnitude of the gyre will be sensitive to the formulation of viscous and diffusive processes. Once again, the GCM results given in the next section will help clarify this.

Estimates of the coastal amplitudes of the baroclinic signals propagating away from the ridge may be found as in the single- and two-layer models by integrating the continuity equation over the appropriate area and substituting for w from the heat equation, but these will only have limited validity due to the much slower phase speeds of the higher-order baroclinic modes.

c. Amplitudes for uniform stratification

A detailed four-dimensional decomposition of the fields and matching is beyond the scope of this paper, though it is of interest to get some estimate of the magnitude of the first baroclinic mode signal, which will propagate rapidly around the basin and the projection onto the higher-order vertical modes, which propagate more slowly, and in the context of a climate GCM will be poorly resolved spatially and just dissipate in the neighborhood of their generation.

If we assume that the background stratification is of the form

$$\rho_B = \exp(-z/D_S),$$

where D_S is assumed large compared with D_O, and large compared with the scale over which the vertical velocity varies, i.e., $(\rho_B w_z)_z \approx \rho_B w_{zz}$, then the vertical eigenfunctions for horizontal velocity are just $\cos(n\pi/D_O)$, see Gill (1982, §6.11). Inclusion of horizontal diffusive processes will not change the structure of the vertical eigenfunctions; neither will vertical diffusive processes, provided these are incorporated in the form described by McCreary (1981). The dimensional offshore decay scale for the nth vertical mode coastally trapped Kelvin wave in the absence of dissipation, i.e., the nth Rossby radius, is

$$a_n = \frac{H_O}{n\pi f}(g/H_S)^{1/2},$$

and so in this case $\gamma_n = \Gamma^2$ for all n.

Assuming $\hat{v}_O$ has the form $\hat{v}_O = \hat{v}_O(x, y, t)\cos(\pi z/D_O)$, then from (3.8)

$$\bar{v}_O = \frac{(\psi_x)_N}{D_O} = \frac{\sin\pi/\Gamma}{\pi(1-\Gamma^{-1})}\hat{v}_O \quad \text{at} \quad y = W+, \quad \Gamma > 1, \quad (3.13)$$

and from (3.7), if $\hat{v}_R = \sum_{n=1}^{\infty}\hat{v}_{Rn}(x, y, t)\cos(n\pi z/D_R)$, then

$$\hat{v}_{Rn} = (-1)^n \frac{2\Gamma\sin\pi/\Gamma}{\pi(1-n^2\Gamma^2)}\hat{v}_O \quad \text{at} \quad y = W-, \quad \Gamma > 1. \quad (3.14)$$

The vertical eigenfunctions describing the depth-confined signal propagating out along the ridge face are $\{\cos n\pi(1 + z/D_R)/(\Gamma - 1)\}$. Therefore, if $\hat{v}_D = \sum_{n=1}^{\infty}\hat{v}_{Dn}(x, y, t)\cos n\pi(1 + z/D_R)/(\Gamma - 1)$, then from (3.9)

$$\hat{v}_{Dn} = (-1)^{n+1}\frac{2(1-\Gamma^{-1})\sin\pi/\Gamma}{\pi\{n^2 - (1-\Gamma^{-1})^2\}}\hat{v}_O. \quad (3.15)$$

At the northwest intersection, if $\hat{v}_E = \sum_{n=1}^{\infty}\hat{v}_{En}(x, y, t)\cos(n\pi z/D_O)$, then from (3.10a, b)

$$\hat{v}_{En} = \frac{2\Gamma}{n\pi}\sin\left(\frac{n\pi}{\Gamma}\right)\bar{v}_E \quad \text{at} \quad y = W+ \quad (3.16)$$

where

$$\bar{v}_E = (\psi_x)_E/D_O.$$

At the southwest intersection, if

$$\hat{v}_S = \sum_{n=1}^{\infty}\hat{v}_{Sn}(x, y, t)\cos(n\pi z/D_R)$$

and

$$\hat{v}_T = \sum_{n=1}^{\infty}\hat{v}_{Tn}(x, y, t)\cos(n\pi z/D_O),$$

then from (3.12a, b)

$$\hat{v}_{Tn} = \frac{\sin n\pi/\Gamma}{n\pi} \times\left\{\sum_{m=1, m\Gamma\neq n}^{\infty}\frac{2(-1)^m}{\{1-(m\Gamma/n)^2\}}\hat{v}_{Sm} + \Gamma(\psi_x)_S\right\} + \Gamma^{-1}\hat{v}_{Sm}\delta_{m\Gamma,n}, \quad (3.17)$$

where $(\psi_x)_S$ denotes ψ_x at $y = -W$, and $\delta_{i,j}$ is the Kronecker delta.

Figure 6 shows the variation of the coefficients for the first five modes as a function of Γ. Figure 6a also includes (3.13), showing the ratio of the barotropic velocity to the incident first baroclinic mode amplitude at $y = W+$ as a function of Γ. It is noteworthy that the solution is discontinuous, since $\psi_x = 0$ for $\Gamma = 1$, i.e., no ridge, but $\psi_x/D_O \to \hat{v}_O$ as $\Gamma \downarrow 1$. The baroclinic signal on the ridge is first mode with amplitude $\hat{v}_O$ for $\Gamma = 1$. As Γ increases, i.e., the height of the ridge increases, the amplitude of the first baroclinic mode on the ridge decreases, though the amplitudes of the other modes remain small; see Fig. 6a and (3.14). The energy associated with the incident first baroclinic mode perturbation is being increasingly deflected along the ridge face, and not transmitted across the ridge, as may be seen in Fig. 6b and (3.15). The along-ridge signal will also have most of its energy in the first baroclinic mode. The ratio $\hat{v}_{En}/\bar{v}_E$, given by (3.16), is shown as a function of Γ in Fig. 6c. The modes are all significant, in-

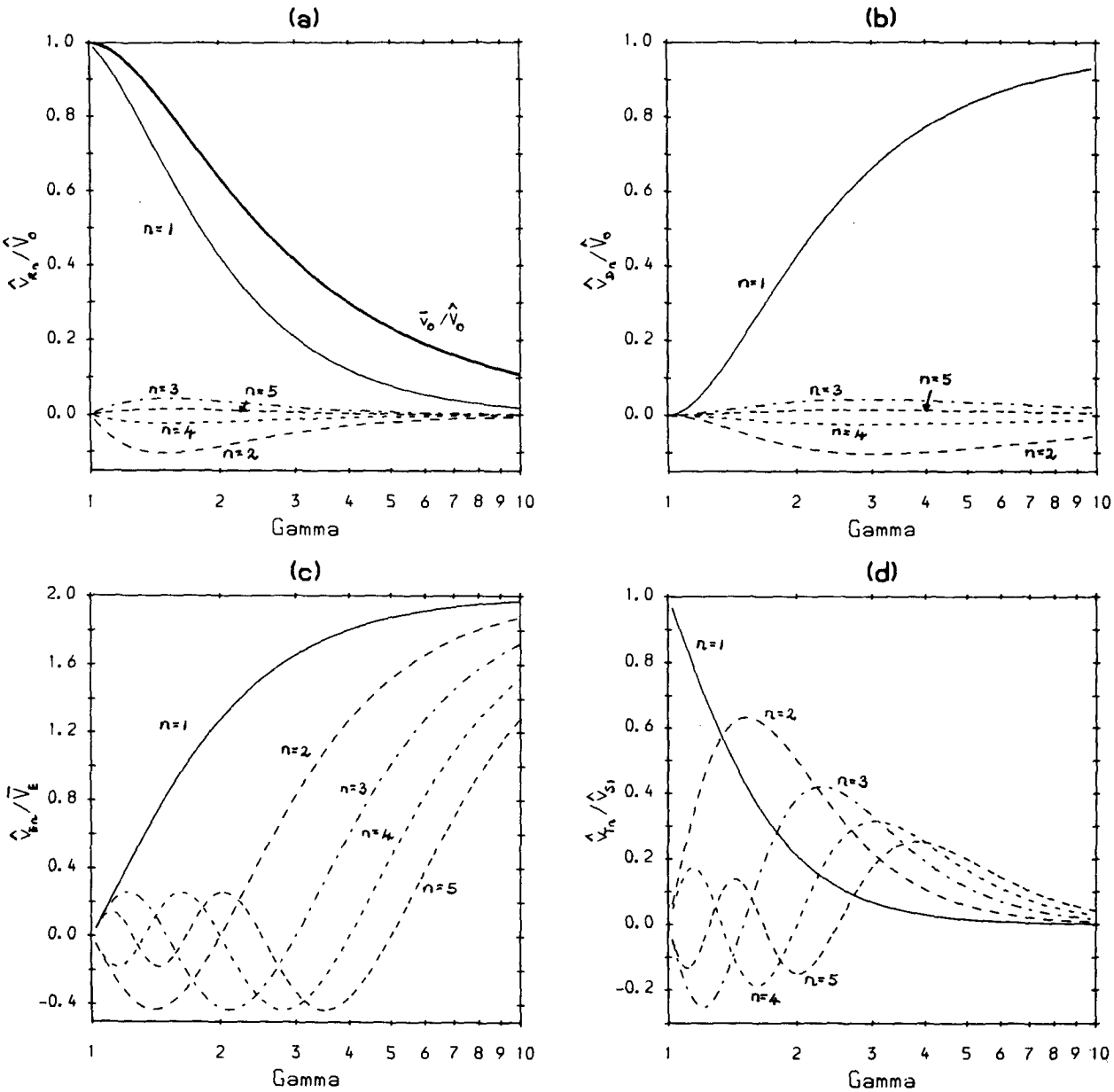

FIG. 6. The ratios $\hat{v}_{Rn}/\hat{v}_O$ as given by (3.14), $\hat{v}_{Dn}/\hat{v}_O$ as given by (3.15), $\hat{v}_{En}/\bar{v}_E$ as given by (3.16), and $\hat{v}_{Tn}/\hat{v}_{S1}$ as given by (3.17) assuming only a first baroclinic mode on the ridge are plotted as functions of Γ in (a), (b), (c), and (d), respectively, for $n = 1, 2, \cdots, 5$. The ratio $\bar{v}_O/\hat{v}_O$ as given by (3.13) is also shown in (a).

dicating that the baroclinic structure at the intersection of the northern ridge edge with the east coast is likely to be quite complex, though for $1.5 < \Gamma < 3$ the first baroclinic mode is dominant. At the southwest corner of the ridge, Fig. 6d illustrates the amplitudes of the modes generated for a first baroclinic mode on the ridge, i.e., $\hat{v}_S = \hat{v}_S \cos(\pi z/D_R)$ in (3.17), assuming the barotropic amplitude is negligible. In this case, the dominant mode south of the ridge is that for which $n \sim \Gamma$.

4. Results from a multilevel general circulation model

An 18-level general circulation model (GCM) is used to illustrate and investigate further the adjustment processes described in the previous section. A full description of the equations and physics may be found in Cox (1984). They are similar to (3.1)–(3.4), except cast in spherical polar coordinates with the nonlinear terms retained. The initial conditions are equivalent to those imposed in the two-layer experiment. The

background stratification is based on that found in the North Atlantic. In the northern third of the basin a horizontally uniform positive potential density perturbation is imposed, which ranges from ~2% at the surface to ~0.1% at depth; details are given in Table 1. It should be noted that the exact details of the basin size and geometry, latitudes spanned, magnitude and structure of the anomaly are not particularly relevant, as this study is really a thought experiment, and the dynamical processes described are quite robust for scales larger than a Rossby radius. A typical meridional baroclinic velocity profile, associated with the coastally trapped signal propagating toward the ridge, and the ridge cross sections considered are shown in Fig. 7a. The vertical eigenfunctions for the first three baroclinic modes, based on a normal mode decomposition with the initial background stratification as described in Wajsowicz and Gill (1986), are shown in Fig. 7b,c for the vertical and horizontal velocities. The simplest formulation of topography in a level model is used. A ridge is represented by a stack of boxes, with boundary conditions such that on the side walls both components of horizontal velocity must be zero and on the top face of the boxes the vertical velocity is zero and the horizontal velocity has no vertical shear, i.e., there is no bottom friction; see Fig. 7d. There is also a boundary condition of no heat flux across any of the faces. The distribution of level depths in the 18-level model corresponds to that which would typically be chosen in a global climate model giving good vertical resolution of the lower-order baroclinic modes.

a. Ridges with a top-hat cross section

The adjustment for a ridge with Γ $(=H_O/H_R)$ $= 1.47$ in which case for the prescribed stratification γ_1 $(=c_{O1}^2/c_{R1}^2) = 1.37$ will be described and compared with that for one with $\Gamma = 2.42$ and $\gamma_1 = 2.37$. The initial adjustment proceeds as expected from the previous experiments. A coastally trapped cold anomaly propagates toward the ridge, with a quite broad front arriving after about 12 days, and the upwelling maximum after about 18 days. This implies a wave speed for the front of 0.8 m s^{-1}, compared with a first baroclinic mode, gravity wave speed associated with the background stratification of 2.65 m s^{-1}. Hsieh et al. (1983) predict that coastally trapped Kelvin waves, with wavelengths $\leqslant 20°$ of latitude, propagating in a medium with lateral viscosity coefficient, $A_M = 5 \times 10^4$ m^2 s^{-1}, and lateral diffusivity coefficient, $A_H = 5 \times 10^3$ m^2 s^{-1}, and horizontal grid resolution of 1° of latitude, will be nondispersive and have a phase speed reduction of about one-third, in agreement with that above.

TABLE 1. Model depths and initially prescribed stratification.

Depth (m)	Potential temperature (°C)	Potential density (g cm^{-3})
7.5	21.0	24.547
25.0	19.0	25.034
47.5	18.0	25.266
90.0	16.4	25.621
150.0	14.0	26.117
220.0	13.4	26.234
340.0	12.4	26.423
500.0	11.0	26.674
665.0	9.88	26.864
880.0	8.37	27.104
1145.0	6.63	27.357
1415.0	5.95	27.450
1715.0	5.22	27.545
2047.5	4.41	27.645
2382.5	4.20	27.670
2750.0	3.86	27.710
3150.0	3.50	27.751
3550.0	3.14	27.791

1) ADJUSTMENT AT NORTHERN RIDGE EDGE

The barotropic streamfunction is shown at 60 days in Fig. 8, for the model with $\Gamma = 1.47$. The structure is similar to the two-layer model, consisting of a basinwide anticyclonic gyre, with a maximum of 9.8 Sv, centered on the northern ridge edge and a cyclonic gyre, with a minimum of −0.98 Sv, confined to the western boundary layer on the southern ridge edge. In section 3, it was deduced that the magnitude of the anticyclonic gyre would be such as to give zero net vertically integrated transport over the depth of the ridge. Calculations based on the fields, which are one grid point, i.e., 1° of latitude, north of the ridge, confirm (3.6) and (3.8). From (3.8), for a typical first baroclinic mode structure, the interior value of ψ should be reduced for a higher ridge. For the $\Gamma = 2.42$ model, ψ_I is only 8.8 Sv at 60 days.

In the previous sections, models with uniform rotation have been considered. If f varies with latitude (or y on a β plane), then for a ridge with a continuously differentiable profile, the JEBAR effect would give

$$(\nu - 1)\psi_x \approx -\left\{\int_{-D}^{0}\int_{z}^{0} \rho_x dz'dz - D\int_{-D}^{0}\rho_x dz\right\} \tag{4.1}$$

over y for which $D_y \neq 0$, where $\nu = (\beta H)/(fH_y)$, where β is the meridional planetary vorticity gradient. If the topographic gradient dominates the planetary vorticity gradient, i.e., $0 < \nu \ll 1$, then the adjustment is such that the total meridional velocity is zero at $z = -D$ to a first approximation. In the GCM, see Cox (1984), if the grid spacing is r degrees of latitude and the depth changes by a fraction $1/\Gamma$ over this distance at a latitude θ°N, then

$$\nu = \frac{(\Gamma + 1)}{(\Gamma - 1)}\frac{\tan(r/2)}{\tan\theta}. \tag{4.2}$$

For $\Gamma = 1.47$, $\theta = 45$°N, and $r = 1°$ of latitude, the above gives $\nu = 0.04$. Rearranging (4.2), the maximum

grid-box thickness over which the topography may vary over a grid point to give $\nu = 1$ is

$$\frac{\Delta z}{H} = 2\left\{1 + \frac{\tan\theta}{\tan(r/2)}\right\}^{-1},$$

which for the above example with $H = 3750$ m, is ~65 m, and for $H = 1550$ m, $\Delta z_{\max} \sim 27$ m; obviously, the farther north, the smaller the boxes required, and similarly if the horizontal resolution is finer. This result should be borne in mind when modeling the circulation over continental shelves, and other regions where one may expect the planetary vorticity gradient to dominate the topographic gradient.

The meridional velocity and upwelling fields along the west coast at 60 days are shown in Fig. 9 for the model with $\Gamma = 1.47$, and at 120 days in Fig. 10 for the model with $\Gamma = 2.42$. The total meridional velocity is continuous across the northern ridge edge at the surface, though the contours are slightly cusped at levels near the top of the ridge. Lateral viscous and diffusive processes soon smooth out these gradients. For a finite-difference formulation, the variables are not defined on either side of the ridge edge, i.e., at $y = W\pm$. Therefore, the baroclinic meridional velocity cannot be described as discontinuous across the edge as predicted in (3.7)–(3.8). However, Fig. 9b does show that there is a sharp change in $\hat{v}$ between 45°N and 46°N.

In the two-layer model, the amplitude of the interfacial perturbation was unchanged to first order as it propagated onto and across the ridge. Figure 11 shows horizontal sections of potential temperature at model-level depths from 880 m downward for the model with $\Gamma = 1.47$, i.e., the ridge top is at 2550 m. Above 900 m there is little indication of the underlying topography; however, as one goes deeper, the temperature signal on the ridge is increasingly reduced from that incident on it. For the level above the ridge top, there is almost no signal on the ridge. The reduction in temperature anomaly is readily explained by looking at the meridional section for vertical velocity shown in Fig. 9c, and noting that the dominant balance in the heat equation is found to be the temperature change due to vertical advection, as one would expect for coastally trapped Kelvin wave dynamics. The energy associated with the first baroclinic mode signal incident on the ridge is mainly transferred to the first baroclinic ridge mode, as predicted by (3.14), and so the vertical velocity field on the ridge at depths below about 1500 m is much less than at a corresponding depth north of the ridge.

A normal mode decomposition, as described in Wajsowicz and Gill (1986), of the actual meridional velocity field shown in Fig. 9 with the local stratification gives that $\hat{v}_{O2}/\hat{v}_{O1} \sim -0.026$, i.e., the energy in the coastally trapped Kelvin waves initially incident on the ridge is chiefly in the first baroclinic mode, and that $\hat{v}_{R1}/\hat{v}_{O1} \sim 0.99$ and $\hat{v}_{R2}/\hat{v}_{R1} \sim -0.12$, i.e., the energy is almost wholly transferred into the first baroclinic ridge mode. For the model with $\Gamma = 2.42$, not shown, a similar decomposition gives that $\hat{v}_{R1}/\hat{v}_{O1} \approx 0.85$ and $\hat{v}_{R2}/\hat{v}_{R1} \sim -0.21$, almost twice that in the $\Gamma = 1.47$ model. This is in general agreement with the result expressed in (3.14) and Fig. 6a.

For the levels that intersect the ridge, i.e., below 2550 m, there is some indication that the temperature contours have started to curve into the interior by the ridge edge, giving a slight northward gradient in temperature; see Fig. 11. The further along-ridge adjustment has a more definite signature in the vertical velocity field. Figures 12a,b show zonal sections of w at 0.5°, 1.5° of latitude north of the step. The upwelling by the ridge face penetrates farther into the interior at the west coast below the depth of the topography than farther north. However, penetration into the interior does not persist; compare Figs. 12b and 12c. As discussed in section 3, the further baroclinic adjustment required at the ridge face to remove the residual shear seems to take the form of a Kelvin-type wave trapped against the face. The first baroclinic-mode phase speed of an ideal Kelvin wave propagating in the actual stratification between 2550 m and 3750 m, c_D say, is 0.45 m s^{-1}. Therefore, from Hsieh et al. (1983), with resolution $\Delta\,(=\Delta y f/c_D) \sim 25$, all but the very longest waves will be nondispersive and propagate at a reduced (by a factor $\sim \Delta^{-1}$) wave speed of less than 2 cm s^{-1}, or 1° of longitude in 45 days at 45°N. This along-ridge adjustment may be seen much more clearly in the $\Gamma = 2.42$ model, shown in Fig. 13. The amplitude of the upwelling signal propagating into the interior along the ridge face is about the same as that at the coast, consistent with the larger projection onto the first baroclinic mode predicted by (3.15) and shown in Fig. 6b. It is also more obvious that the perturbation is confined to the ridge face and does not penetrate higher. The first baroclinic-mode wave speed, based on the actual stratification between 1550 m and 3750 m is 0.89 m s^{-1}, which for a grid resolution of only $\Delta \sim 13$ is reduced to ~6.8 cm s^{-1}, or 1° of longitude per 14 days at 45°N, which is in good agreement with the speed at which the upwelling maximum is propagating in Fig. 13.

2) Baroclinic response at an east coast

The structure of the velocity fields along the east coast at 60 days for the $\Gamma = 1.47$ model is shown in Fig. 14 and at 120 days for the $\Gamma = 2.42$ model in Fig. 15. Initially, the induced baroclinic response will be small above the top of the ridge and away from the face. In this case, the vertical velocity will decrease linearly from a maximum of $-(1 - \Gamma^{-1})\psi_x/\Delta y$ at $z = -D_R$ to zero at $z = 0, -D_O$. For $\Gamma = 1.47$ and $\psi_x \sim 3$ Sv over 1° of longitude at 45°N, see Fig. 8, the above gives a maximum of $\sim 7.8 \times 10^{-3}$ cm s^{-1}, which is in agreement with the field shown in Fig. 12b. The

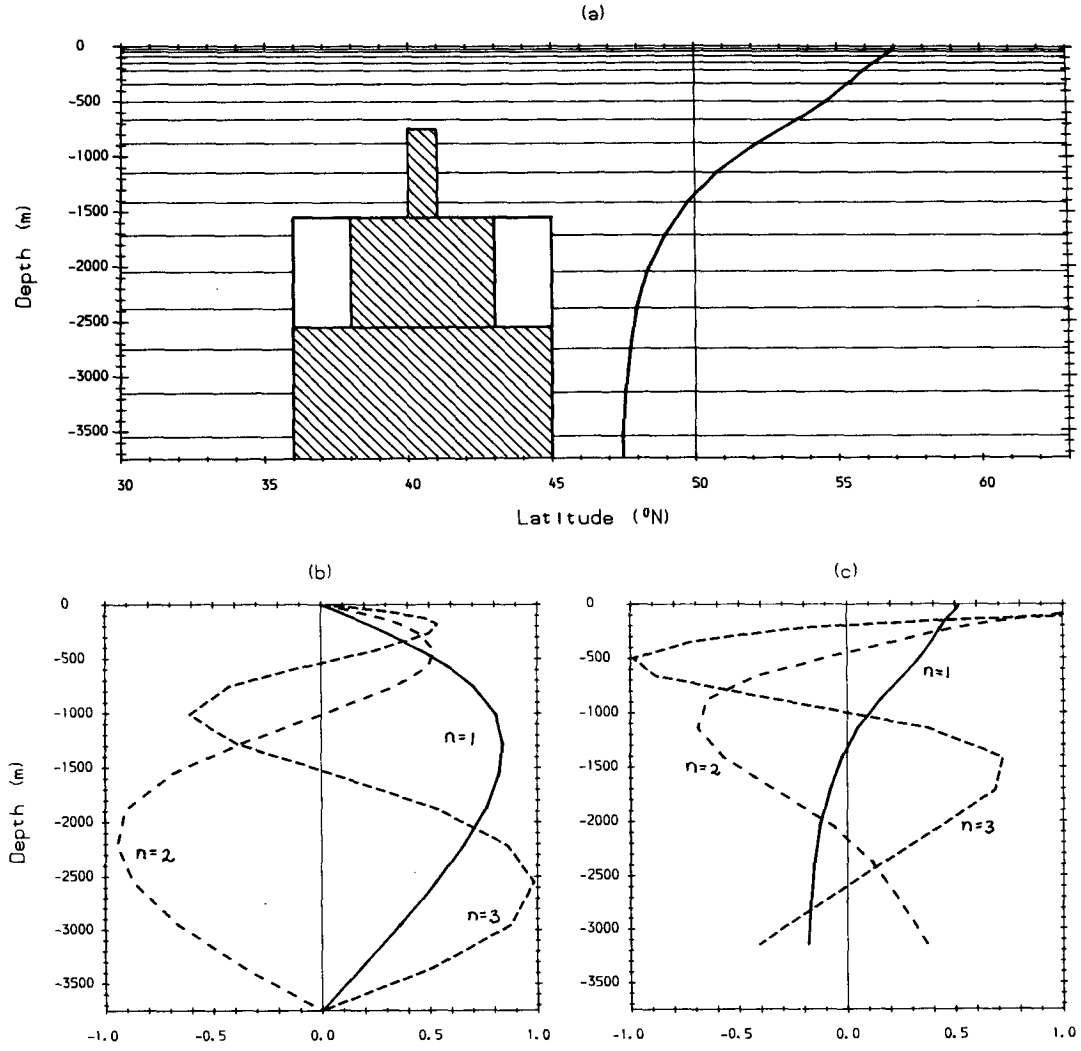

FIG. 7. The meridional extent of the basin, the position and cross section of the three ridges considered, the level depths for the u, v, and T calculations, and a typical meridional velocity profile well north of the ridge are shown in (a). A normal mode decomposition, as discussed in Wajsowicz and Gill (1986), for the initial background stratification, gives vertical structure functions shown in (b) for horizontal velocity profiles, and in (c) for the vertical velocity. The first three modes only are shown. The associated gravity wave speeds are 2.65, 1.29, and 0.903 m s^{-1}. The distribution of the prognostic variables u, v: (O), and T, ψ: (×) in a vertical section are shown in (d); the position of w: (·) used in the T calculation is also shown as it gives the top of any topography, an example of which is denoted by a dotted line.

baroclinic meridional velocity required to give continuity of total velocity across the ridge edge and satisfy the no-normal flow boundary condition, i.e., (3.10), would arise from a density perturbation field $\rho_x \approx -(\psi_x/D_R)\delta(z + D_R)$. In a GCM, it takes about 10 days for the vertical velocity field to evolve from a linearly varying one to one with upwelling concentrated at the ridge top, thus producing an intense density perturbation. Vertical viscosity and diffusion smooth out the sharp profile, though the small vertical extent of the upwelling above the ridge is accentuated by the northward propagation of the weak downwelling field, which has formed on the ridge; see Fig. 14c. The sharp upwelling produced by the southward barotropic flow over the ridge edge generates a sharp meridional gradient in temperature. Horizontal diffusion will lead to this cooling spreading onto the ridge, where it will be countered by a coastally trapped Kelvin wave propagating northward trying to restore the warmer background temperature field by downwelling.

Observations of passive tracers such as tritium are increasingly used to make deductions about the ocean general circulation, e.g., Livingstone et al. (1985), and in GCM studies as a diagnostic tool, e.g., Sarmiento (1983). From the above, with the stacked-box representation of topography, passive tracers would not be readily upwelled from depth onto the ridge by the upwelling field generated. Even if w decreased only lin-

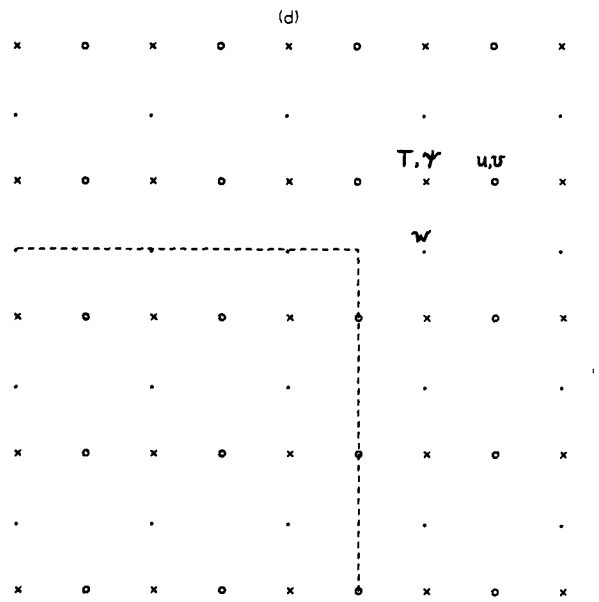

FIG. 7. (Continued)

early with depth below the ridge top, the time taken for a passive tracer to be upwelled to the level of the ridge top would be logarithmic, i.e., if $w = (dz/dt) = w_{\max}(1 + z/D_O)(1 - \Gamma^{-1})^{-1}$, then $t \sim (D_O/w_{\max})(1 - \Gamma^{-1}) \ln\{(1 - \Gamma^{-1})/(1 + z/D_O)\}$, so it would take about a year to be upwelled 1000 m from $z = -3550$ m to the ridge top, and forever from $z = -D_O$. If the ridge had a smoothly differentiable cross-section profile $z + D_S(y) = 0$, passive tracers at $z = -D_S$ would have vertical velocity $-vD_{Sy}$, and thus would be more readily upwelled over some initial phase before a significant baroclinic circulation developed.

In the $\Gamma = 2.42$ model, a weak downwelling develops alongside the sharp upwelling; see Fig. 13. For the $\Gamma = 1.47$ model, a good estimate of w at $y = W+$ (i.e., 45.5°N), $-D_R \geq z \geq -D_O$ is given by $-\psi_x(1 + z/D_O)/\Delta y$, assuming that there has been negligible propagation of the baroclinic signal northward, i.e., $\hat{u}$, $\hat{v}$ at 46°N are very much less than ψ_x/D_O at 45.5°N, as the projection will chiefly be onto the higher-order baroclinic modes. In the $\Gamma = 2.42$ model, however, by 120 days a similar estimate is too large by a factor of two. The baroclinic velocity is no longer negligible compared with the barotropic velocity as the projection onto the northward-propagating first baroclinic mode is much greater, as predicted by (3.15); see Fig. 15. The offshore decay scale of the baroclinic signal is greater than the width of the viscous barotropic boundary layer, and so there is northward flow, and hence downwelling outside this layer.

A normal mode decomposition of the actual baroclinic meridional velocity field north of the ridge at the east coast for the $\Gamma = 1.47$ model gives that $\hat{v}_{E1}/\hat{v}_{O1} \sim -0.18$ and $\hat{v}_{E2}/\hat{v}_{E1} \sim -0.5$, which is in good agreement with that predicted by (3.16) and Fig. 6c. The first baroclinic mode will propagate as a coastally trapped Kelvin wave up the eastern boundary about twice as fast as the second mode. The horizontal resolution is sufficiently coarse that the wave speeds of the higher mode Kelvin waves are very small, so we would expect a more complicated vertical structure to be confined to the vicinity of the ridge, which may be seen in Fig. 14b. A similar decomposition for the $\Gamma = 2.42$ model gives that $\hat{v}_{E1}/\hat{v}_{O1} \sim -0.48$ rising to ~ -0.52 as the flow field develops, which is 2.8 times that in the $\Gamma = 1.47$ model. The ratio $\hat{v}_{E2}/\hat{v}_{E1} \sim -0.22$, which is about half that in the $\Gamma = 1.47$ model, but this increases to ~ -0.5 with time.

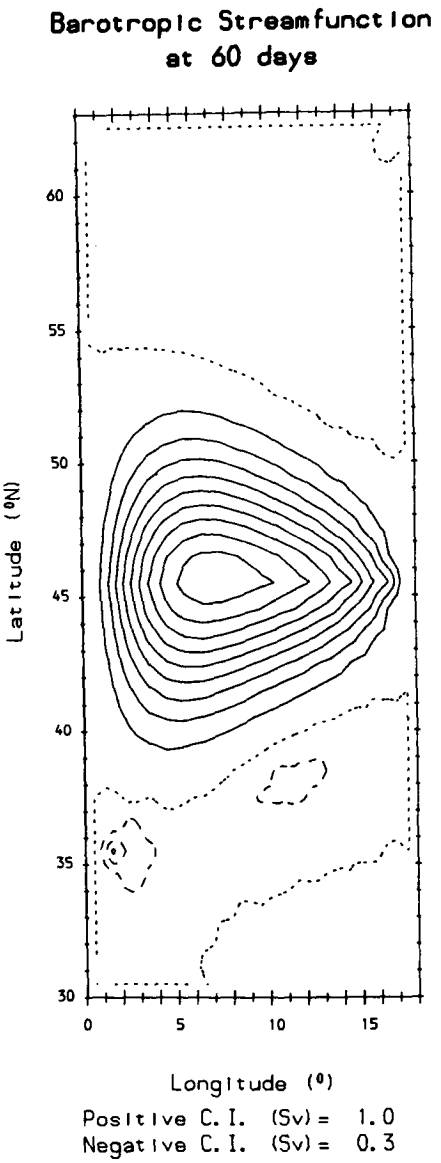

FIG. 8. The barotropic streamfunction for a top-hat ridge between 36°N and 45°N and of height 1200 m. The contour interval is different for the positive (solid) and negative (dashed) contours to show the structure of the cyclonic gyre centered at the southwest ridge edge. The zero contour is denoted by a dotted line.

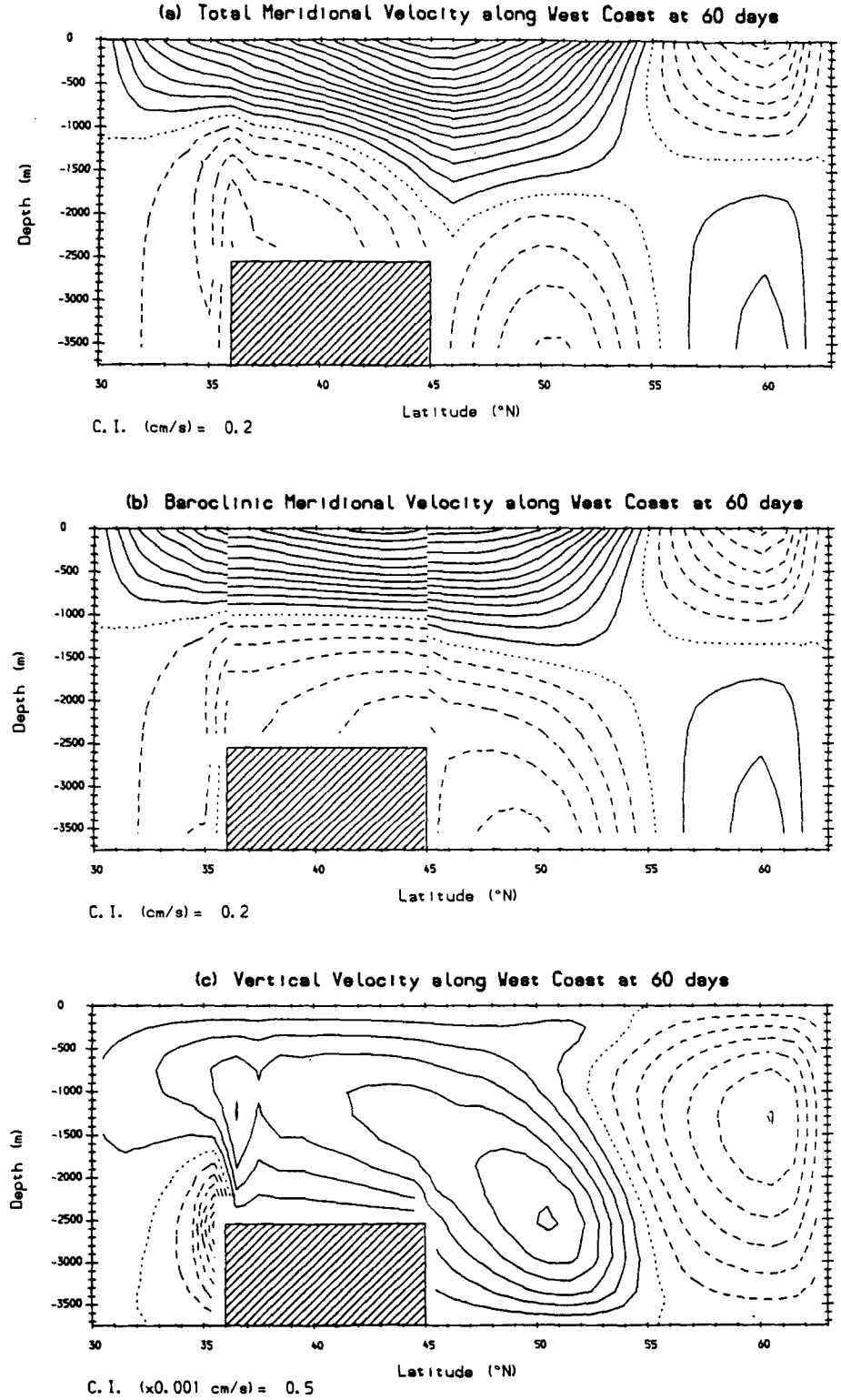

FIG. 9. Contour maps of the total and baroclinic meridional velocities for 1° of latitude in from the west coast and vertical velocity, as used in the prognostic temperature equation, for ½° of latitude in from the west coast are shown in (a), (b), and (c), respectively, at 60 days, i.e., ~45 days after the Kelvin wave front encounters the ridge. The contour interval is given at the bottom of each map, and the same line style scheme as Fig. 8 is used. The ridge cross section is also shown. The boundary conditions at the corners are not defined, see Fig. 7d, the contours in the box surrounding these

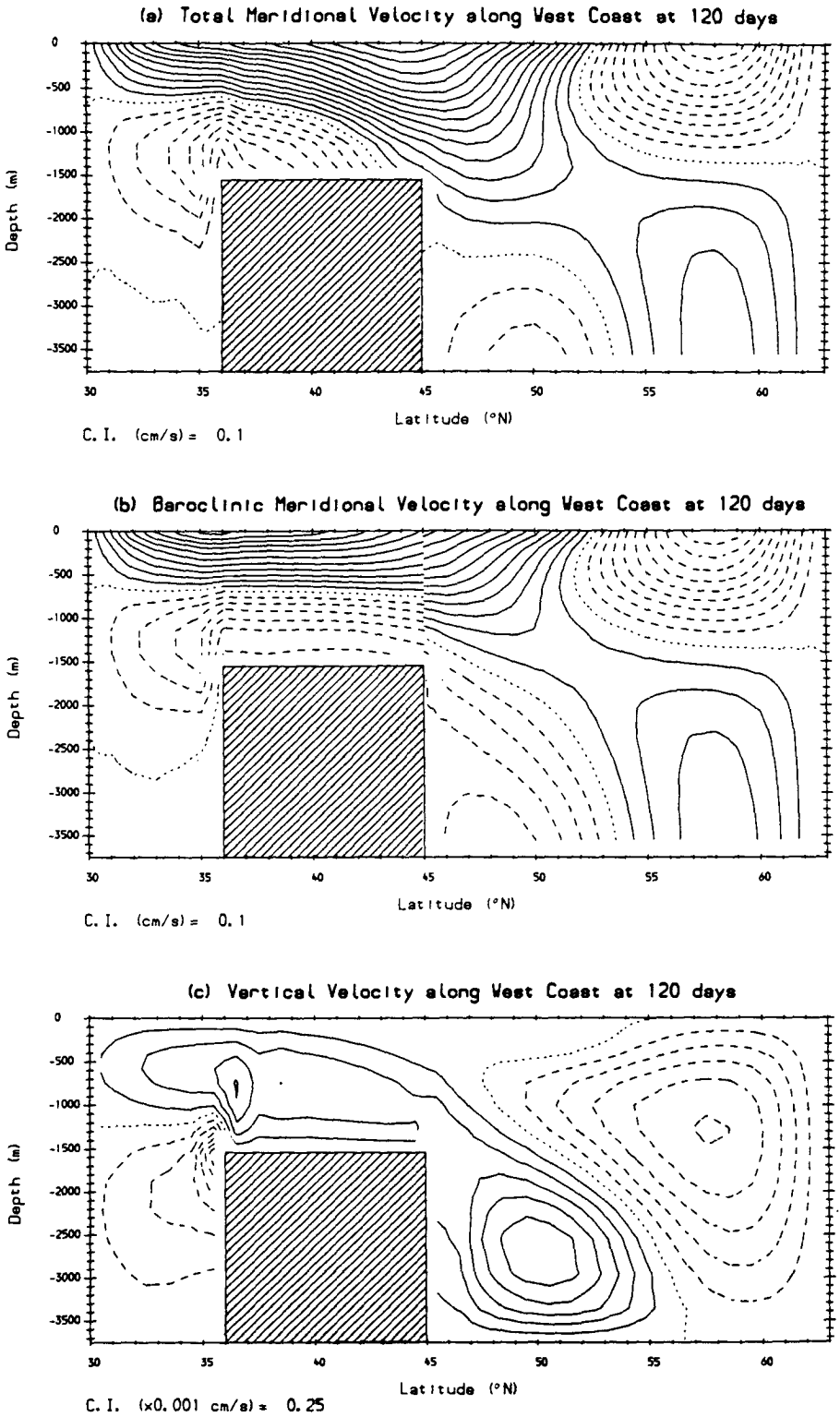

FIG. 10. As for Fig. 9, but for the model with a ridge of height 2200 m, i.e., $\Gamma = 2.42$, at 120 days.

points are not drawn. The baroclinic velocity is calculated as the total minus the depth averaged, which is taken as that over the depth of the ridge at 36°N and 45°N. If the total meridional velocity is continuous across the ridge edge, then the baroclinic meridional velocity must be discontinuous there. This is illustrated in (b), though due to the staggered-grid formulation of the model, such a discontinuity does not arise explicitly.

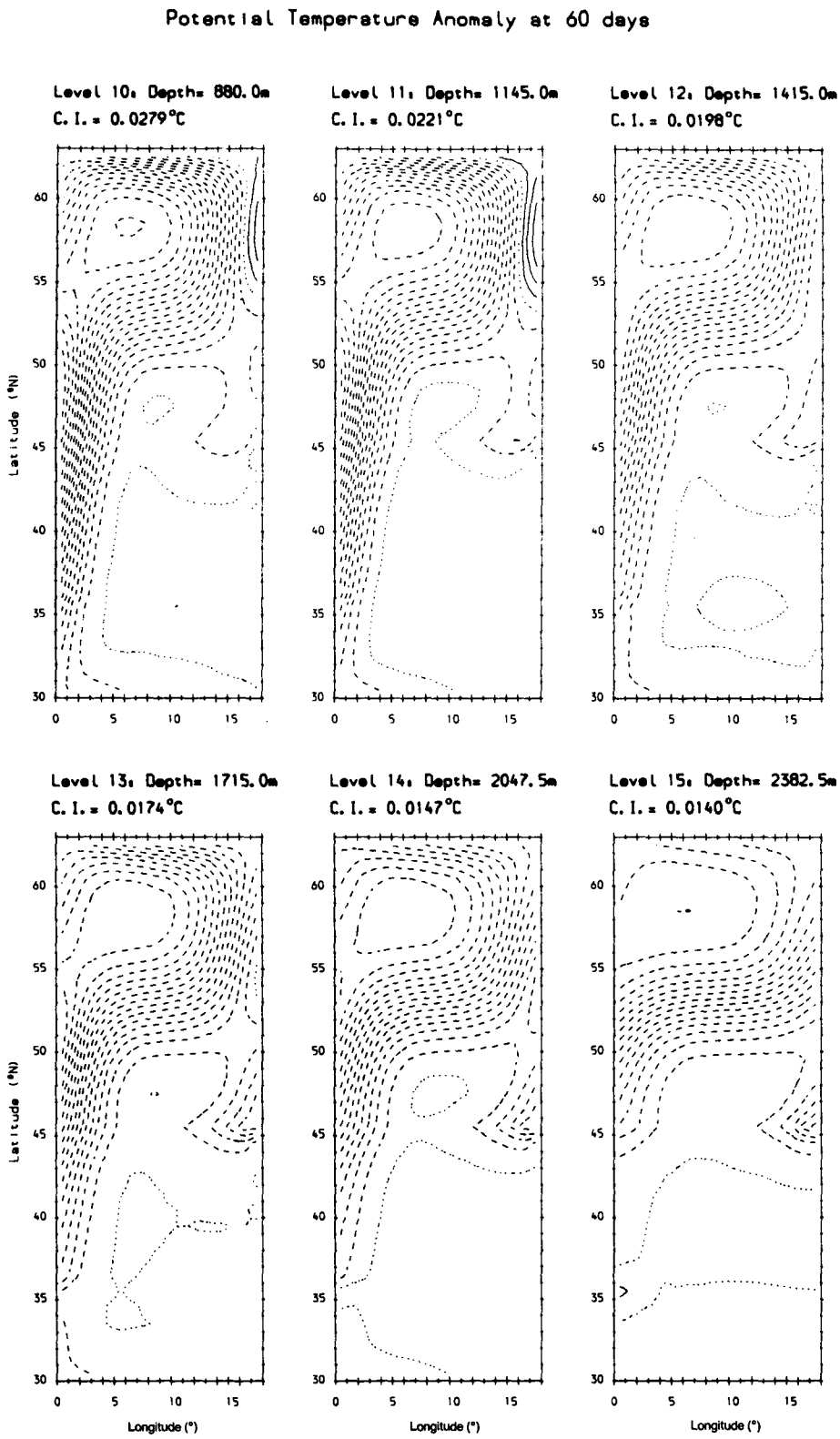

FIG. 11. Contour maps of the potential temperature anomaly at level sections of the model with $\Gamma = 1.47$ below 750 m are shown at 60 days. The contour interval below 2500 m is $^1/_{40}$th that of the initial anomaly at a particular depth and above 2500 m the interval is $^1/_{30}$th.

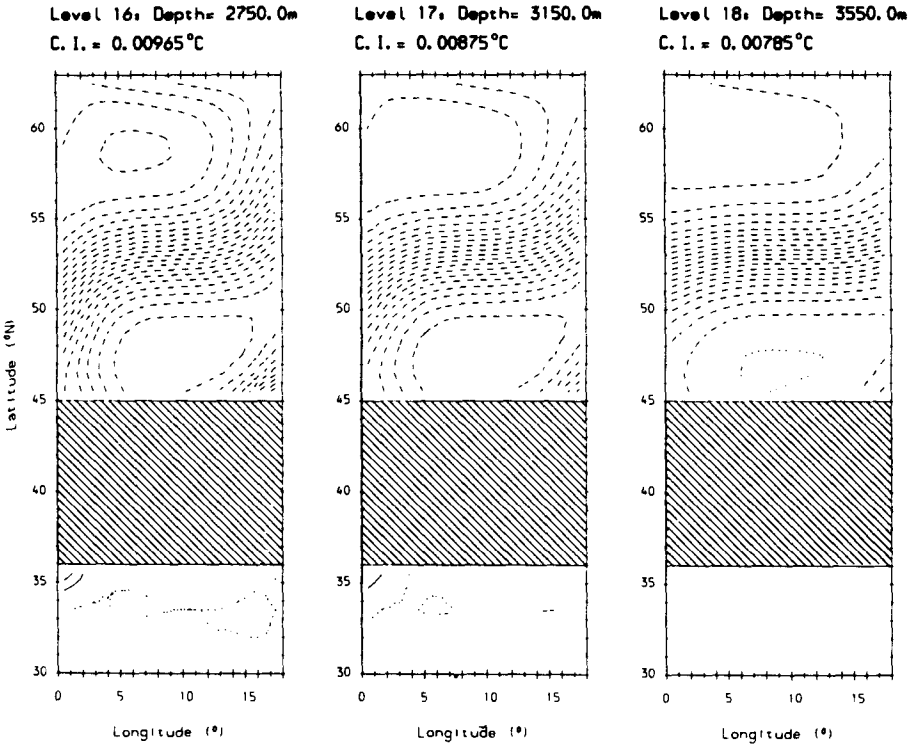

FIG. 11. (*Continued*)

3) ADJUSTMENT AT SOUTHERN RIDGE EDGE

As in the two-layer model, there is a weak cyclonic gyre centered on the edge and confined to the west coast. The potential temperature perturbation field shows a frontal development similar to that found in the interfacial height field; see Fig. 11 for the model with $\Gamma = 1.47$. The negative temperature perturbation propagates seemingly unaffected by the underlying topography above ~900 m. Below this depth, it becomes increasingly pinched, forming quite a distinct front by ~1700 m. The temperature perturbation is positive below the depth of the ridge. From Fig. 9c, the upwelling signal is intensified just north of the ridge edge (cf. the northern ridge edge at the east coast, Fig. 15c) and then continues at about its previous magnitude south of the ridge. There is a sharp downwelling at the ridge edge, which extends to the ocean bottom and also up to ~1700 m, accounting through (3.1e) for the reduction and change in sign of the temperature perturbation. In the $\Gamma = 2.42$ model, Fig. 10c, the downwelling does not penetrate much below 2000 m.

In the two-layer model, the strength of the cyclonic gyre was sufficient to produce effectively zero net lower-layer flow over the outer portion of the baroclinic western boundary layer, and an intense lower-layer flow off the ridge by the coast; see Fig. 5. In the GCM, a sufficient zonal gradient in ψ does not develop to give continuity in v_z across $z = -D_R$ (i.e., $v = 0$ at $z = -D_R+$) over some outer extent of the baroclinic western boundary layer. The sharp downwelling at $z = -D_R$ extends from a maximum at the coast to a couple of degrees into the interior. Nonlinear terms are present in the GCM's momentum equations, but they do not appear to have a significant effect on the dynamics at the stepdown, and the magnitude of the cyclonic gyre appears to be limited by viscous and diffusive effects. A weak baroclinic flow will be generated below the top of the ridge to cancel the weak barotropic flow at the ridge face. There will also be penetration of the circulation below the top of the ridge due to vertical viscous and diffusive processes. The motion generated by both mechanisms is obviously much less than if the cyclonic gyre were stronger, thus, creating a larger, narrower (~ a gridpoint wide) flow off the ridge next to the coast. The comments made earlier about upwelling tracers onto the ridge at the northeast corner apply here also. The lack of penetration of the downwelling will mean that sinking will be increasingly timely with depth, and tracers are likely to be advected southward away from the influence of the downwelling at the ridge before sinking appreciably.

The model in the last part of section 3 was based on the idea that the perturbation fields in each basin could be decomposed into vertical normal modes with the horizontal and temporal structure of each mode governed by the shallow-water equations with differing Rossby radii. This idea was quite successful in explaining the vertical structure of the coastally trapped signals propagating onto the ridge at the west coast and away

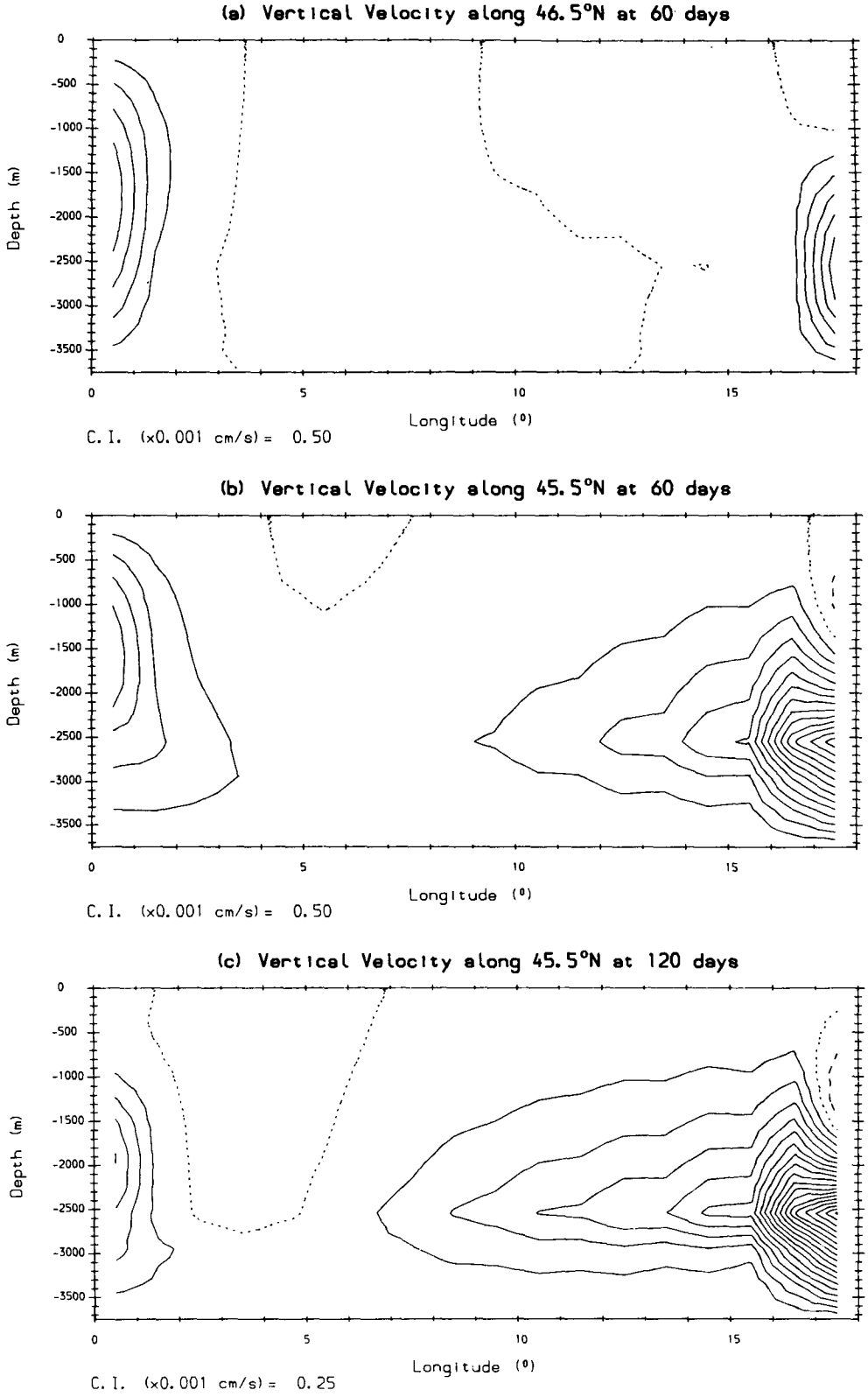

FIG. 12. Latitudinal sections of the upwelling field for the model with $\Gamma = 1.47$ are shown 1.5° of latitude north of the ridge at 60 days in (a), and at 0.5° of latitude north of the ridge at 60 days in (b), and 120 days in (c).

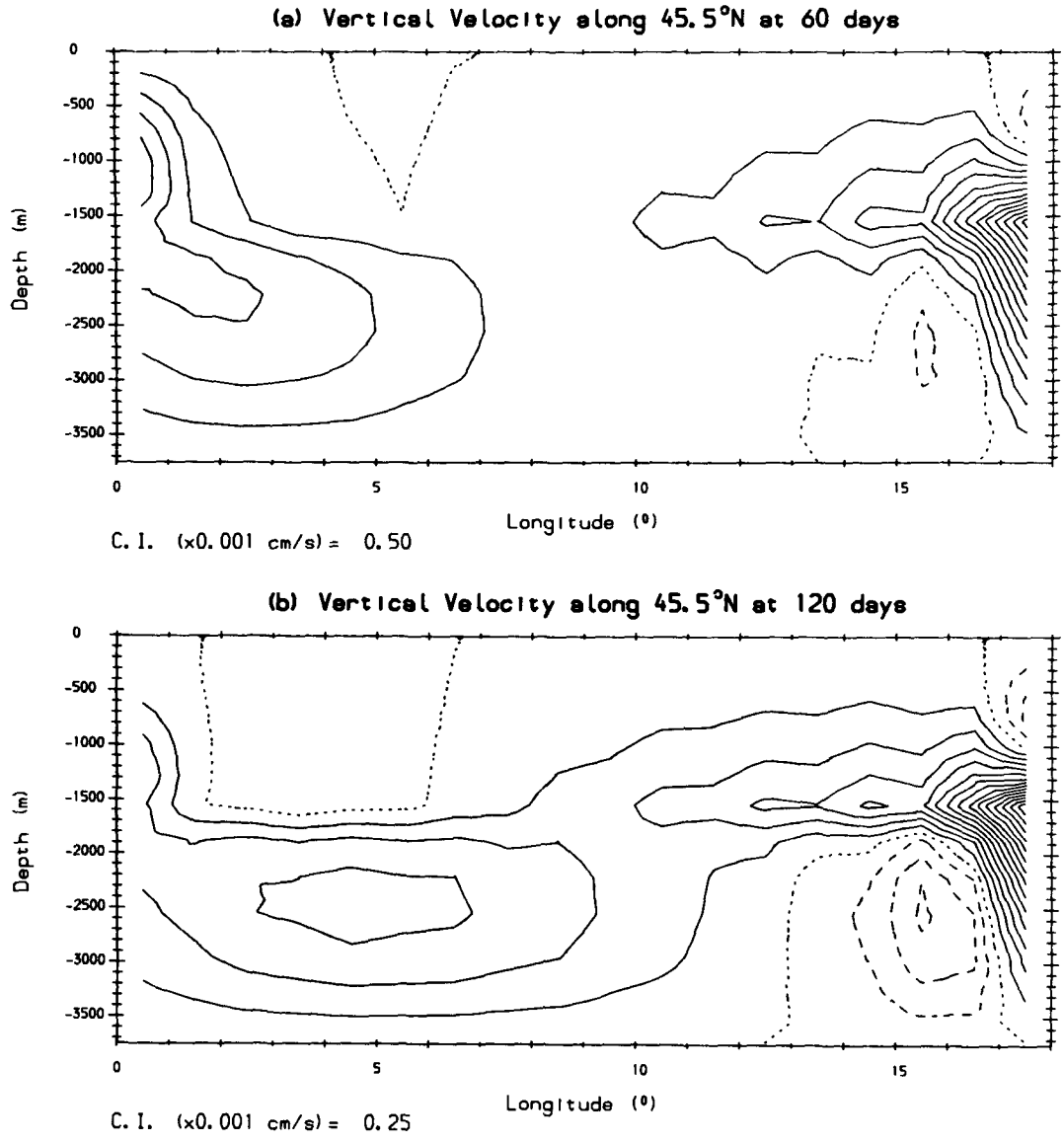

FIG. 13. As in Fig. 12, but for the model with $\Gamma = 2.42$.

from the ridge along the east coast. South of the ridge, one can also observe the different modes propagating along the west and south coasts; see Fig. 16. A normal mode decomposition of the actual field for the $\Gamma = 1.47$ model, shown in Fig. 9a, gives that $\hat{v}_{T1}/\hat{v}_{S1} \sim 0.79$ and $v_{T2}/\hat{v}_{T1} \sim 0.14$. The reduced importance of the second mode in the GCM, compared with that predicted in (3.17) and Fig. 6d, is due to the lack of symmetry in the vertical structure of the modes, see Figs. 7b and 7c. For the $\Gamma = 2.42$ model, the adjustment at the southern ridge edge at the west coast is once again such that the signal on the ridge propagates almost undisturbed across the step down. The minimum of the cyclonic gyre is ~ -0.4 Sv at 120 days, giving a southward barotropic flow next to the coast on the ridge of ~ 0.09 cm s^{-1}. A normal mode decomposition of the field, shown in Fig. 10a, gives that $\hat{v}_{T1}/\hat{v}_{S1} \sim 0.64$, and that $\hat{v}_{T2}/\hat{v}_{T1} \sim 0.68$ compared with $\hat{v}_{S2}/\hat{v}_{S1} < -0.01$, which is about 4.5 times that for the $\Gamma = 1.47$ model and is in agreement with the general result of (3.16) that the higher the ridge the greater the energy in the higher-order modes.

4) ZONALLY AVERAGED TRANSPORT

So far, the emphasis has been on the three-dimensional circulation. For climate studies, the zonally averaged meridional transport is also of interest, since it gives the magnitude of the thermohaline circulation. The associated streamfunction, Ψ, is defined by

$$\Psi_z = -\int_0^L v dx, \quad \Psi_y = \int_0^L w dx \qquad (4.3)$$

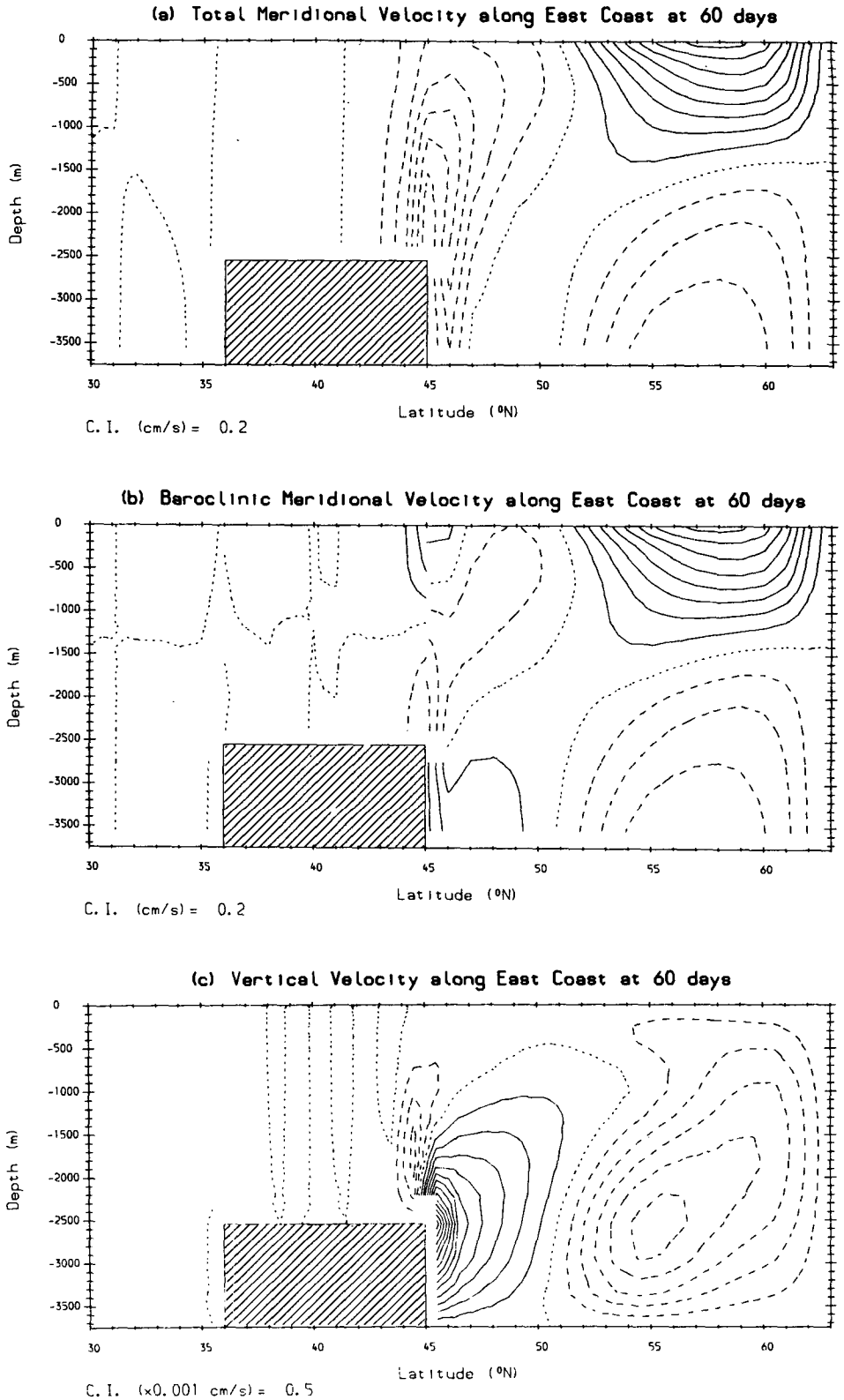

FIG. 14. As in Fig. 9, but now the meridional velocity is shown for 1° of latitude and the vertical velocity for ½° of latitude in from the east coast.

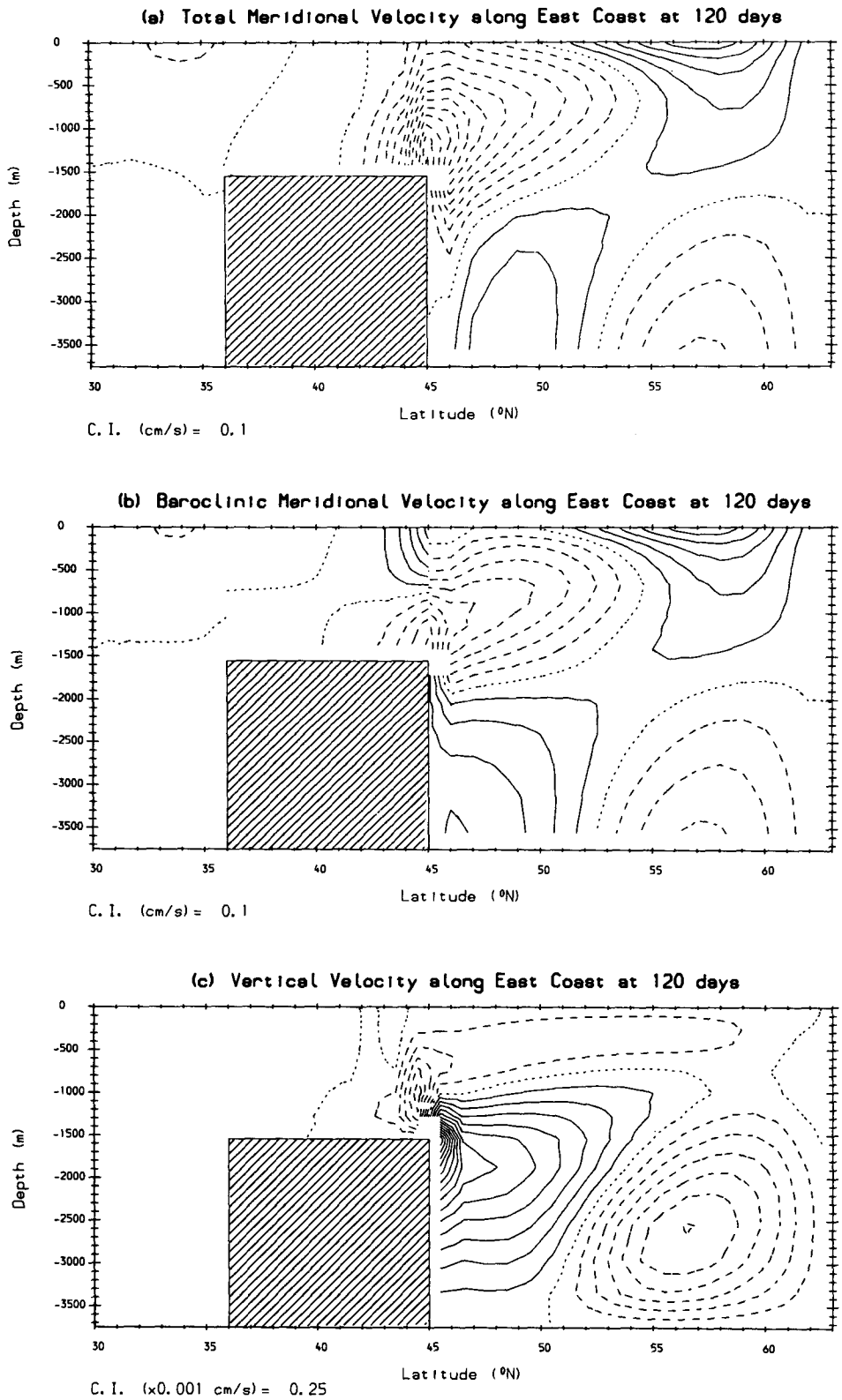

FIG. 15. As in Fig. 14, but for the model with $\Gamma = 2.42$ at 120 days.

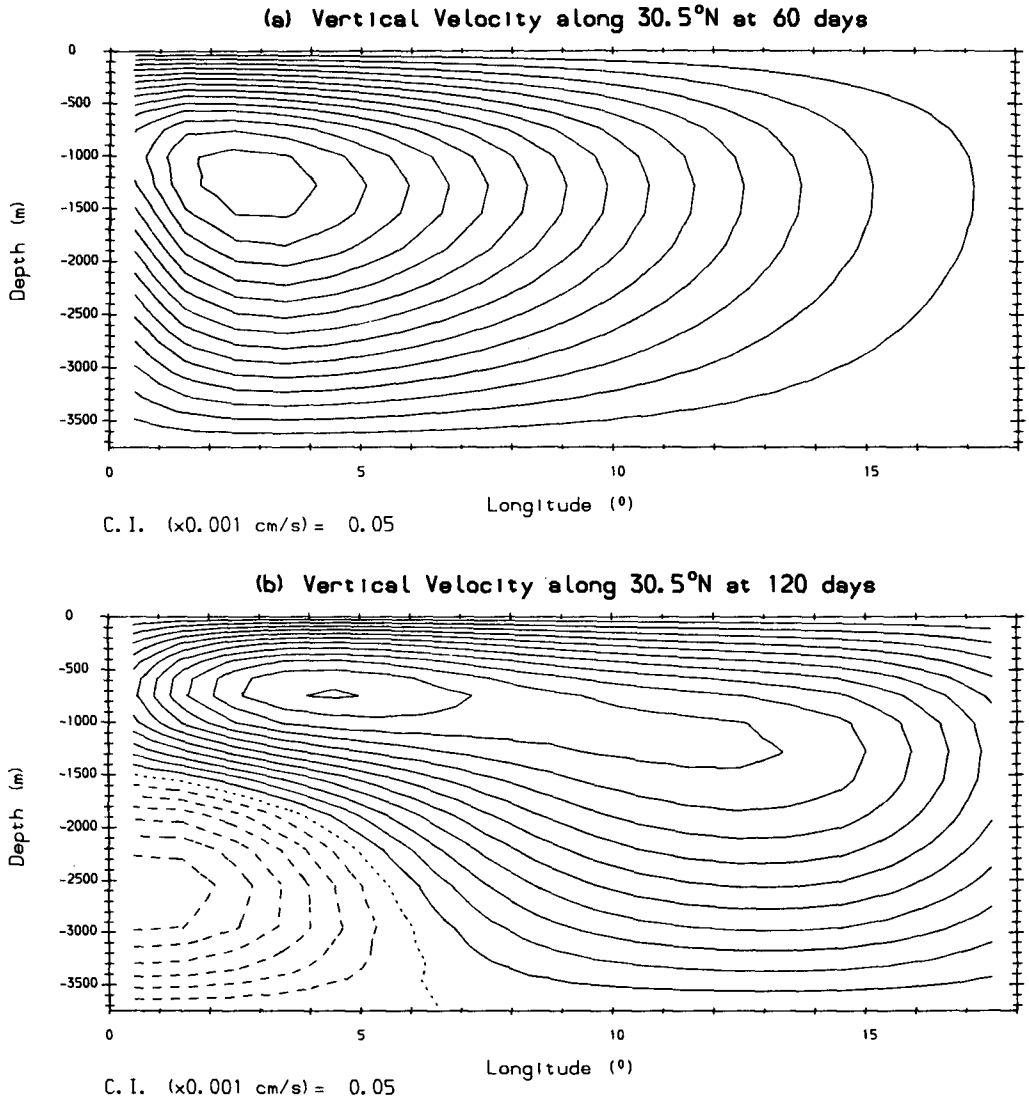

FIG. 16. Latitudinal sections of the vertical velocity along the south coast are shown at 60 days in (a), and 120 days in (b) for the model with $\Gamma = 1.47$.

and its existence is given by zonally integrating the continuity equation (3.1d). In a time-dependent flow, Ψ is not as useful a quantity as in steady-state motions, since the time taken to make a complete circuit of a streamline may well be several hundred years over which time the pattern could have changed significantly, i.e., particle paths and streamlines do not necessarily coincide. However, for an adjustment problem, where only some initial phase is considered as an illustration of the tendency, there is some relevance. In the simple model here, we have just the pseudodevelopment of a classical thermohaline circulation (see Fig. 17) with warm waters moving northward then sinking in the northern region where the initial cold anomaly was sited. The colder water below 1500 m returns southward, where it may be upwelled into the northward flow before it reaches the ridge or, if it is deep enough, it will be upwelled onto the ridge where once again, if it is the deepest water, it will proceed across and sink down the other side. It is of interest to note how little actually sinks—less than a tenth of the total circulation—and also to what depth it sinks: a hundred meters compared with a ridge depth of 1200 m. The time-dependent study carried out here suggests that how much is upwelled and returns northward before crossing the ridge and how much sinks after crossing the ridge is determined by the baroclinic motion generated by the requirement that $v = 0$ at the ridge face, which depends on the magnitude of the barotropic velocity at the northeast and southwest corners of the ridge, and how it projects onto the baroclinic modes, as well as the formulation of viscous and diffusive processes.

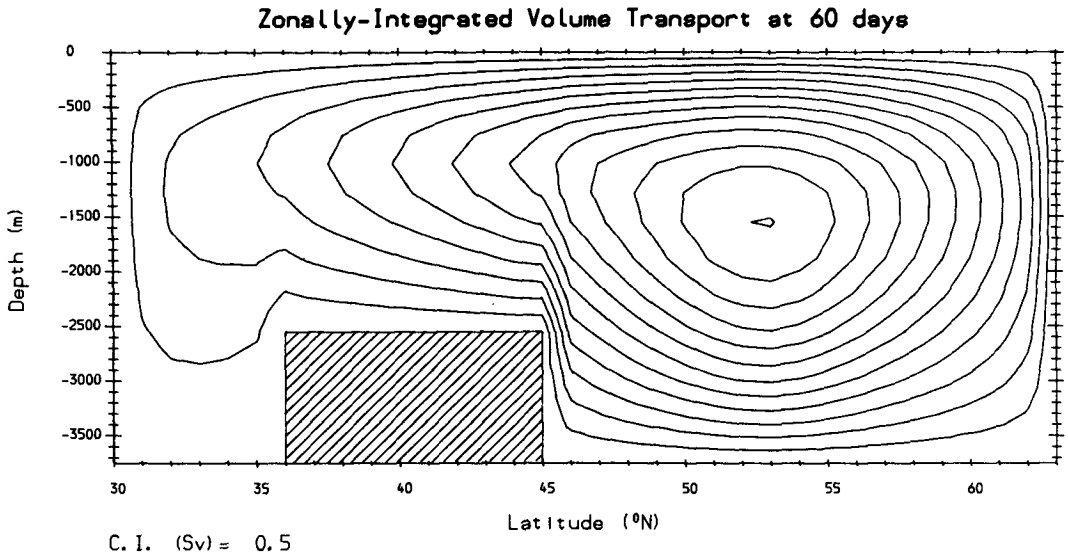

FIG. 17. The zonally integrated transport streamfunction, Ψ, as defined by (4.3), is shown at 60 days for the model with $\Gamma = 1.47$.

An estimate for Ψ may be found by assuming a vertical structure of

$$\begin{matrix}\sin\\ \cos\end{matrix}(n\pi z/H)$$

for the variables as defined earlier in section 3. Integrating with respect to z and using the thermal wind relationship gives in dimensional terms

$$\Psi(z) = \frac{g}{f\rho_o}\frac{H^2}{\pi^2} \times \sum_{n=1}^{\infty} \{\rho_n(x=0) - \rho_n(x=L)\} \sin\frac{n\pi z}{H}.$$

North of the ridge at a given time, it would be expected that Ψ would be less for the $\Gamma = 2.42$ model than that for the $\Gamma = 1.47$ model, because of the greater projection onto the first baroclinic mode at the east coast giving a reduced east–west density contrast. This is found to be the case, with a maximum at 53°N of 4.95 Sv compared with 6.02 Sv, and a maximum 1° of latitude north of the ridge of 2.34 Sv compared with 4.24 Sv at 60 days, respectively. South of the ridge, the confinement of the circulation to above the ridge top is evident. In the $\Gamma = 2.42$ model, by 120 days when the flow is fully developed across the ridge, a weak closed countercirculation has developed below the ridge top, extending from the ridge to the south coast, which brings water northward along the bottom, upwelling it at the ridge face and transporting it southward again just below the depth of the ridge top. The latter circulation reflects the much larger projection onto the second baroclinic mode in this model than the $\Gamma = 1.47$ model.

In the two models considered so far, the top of the ridge has been below the zero-velocity level of the coastally trapped Kelvin waves incident on the ridge at the west coast. Also the ridge cross section has not varied zonally. The modification to the adjustment processes for a higher ridge, which has steps representing a slope, and for one which has more topographic structure (e.g., an island on top of the ridge, cf. Iceland) is of interest and considered briefly in the remainder of this section.

b. A ridge with a pyramid cross section

The cross section is shown in Fig. 7a. It reaches up to 750 m, so $\Gamma_{max} = 5$ and $\gamma_{1max} = 6.15$. The two lower steps were at the same depths as the previous two model ridges. The center of the anticyclonic barotropic gyre is on the first step of the ridge, and the magnitude is about the same as that for the $\Gamma = 1.47$ model. The barotropic streamfunction decreases southward with latitude, such that (3.8) applies at each of the other two step-ups. The baroclinic meridional velocity field is dominated by the appropriate first mode on each step-up. As expected, there are significant upwelling perturbations propagating into the interior along the upper two faces, where the vertical shear in the incident baroclinic flow is greatest. In section 3, it was predicted that for uniform stratification and a top-hat profile at the east coast, the amplitudes of higher-order baroclinic modes would become increasingly comparable to that of the first baroclinic mode at the east coast as the ridge height increased. For the top-hat ridges described in section 3a, the amplitude of the second baroclinic mode was found to be about half that of the first. For the pyramid model, however, the amplitude of the second mode remains at less than 10% of the first mode just north of the ridge at the east coast. Intense upwelling is generated at each of the step edges as the southward

barotropic flow passes over, and the resulting density perturbation will project differently onto the open ocean baroclinic modes than in the previous top-hat model. Also, the ridge "slope" spans 4° of latitude, so it will take longer for the higher-order modes to contribute to the flow north of the ridge. The first baroclinic mode will be relatively unaffected, even though the ratio of its amplitude to that at the west coast north of the ridge increases by 40% between 60 and 120 days—for the previous models the ratio was quite steady by this time. The ratio $\hat{v}_{E1}/\hat{v}_{O1}$ is about four times larger than that for the $\Gamma = 1.47$ model and ranges from about one to one-and-a-half times larger than that for the $\Gamma = 2.42$ model. This is in general agreement with what could be deduced from (3.16) and implies that the zonally averaged meridional mass transport north of the ridge will be weaker than for the other models. South of the ridge, the meridional velocity is very surface-trapped, and it is hard to identify a cyclonic gyre in the noise of the barotropic streamfunction field. A normal mode decomposition of the meridional velocity field gave that just south of the ridge $\hat{v}_{T2}/\hat{v}_{T1} \sim 0.83$, with the third baroclinic mode becoming increasingly important as time progressed: $\hat{v}_{T3}/\hat{v}_{T1} \sim 0.3$ by 180 days. This is in general agreement with (3.17).

c. *A ridge with a top-hat cross section and an island*

The position of the island (cf. Iceland) is shown in Fig. 18, which is of the barotropic streamfunction at 60 days. The main ridge is positioned as before and reaches up to −1550 m, i.e., $\Gamma = 2.42$. The island partially blocks the baroclinic western boundary current that would otherwise develop across the ridge and also the southern part of the barotropic anticyclonic gyre. The island's meridional length scale is comparable with that of the ridge, so that the boundary layers associated with both barotropic and baroclinic flow around the island feel the ridge edges. A full discussion of the adjustment is given in Wajsowicz (1991), which also compares the flow field around an island submerged to different depths. Noteworthy features for this study, however, are the northwestward shift (by about 1° of latitude) and reduction in magnitude (by about 1 Sv) of the anticyclonic barotropic gyre and the O(1 Sv) flow, which crosses off the southern ridge edge. It crosses back onto the ridge in the baroclinic western boundary, thus preventing a cyclonic gyre from developing until about 100 days into the integration. These features lead to a difference in upwelling fields at the ridge edges, which in turn lead to a difference in zonally integrated transport. At 60 days, it is two–three times greater over most of the latitudes south of the ridge, reaching a maximum of over four times greater at the southern ridge edge. Baroclinic flow south of the ridge is established much more rapidly in the island model as a result of the interaction between the anticyclonic barotropic gyre and the southern ridge edge.

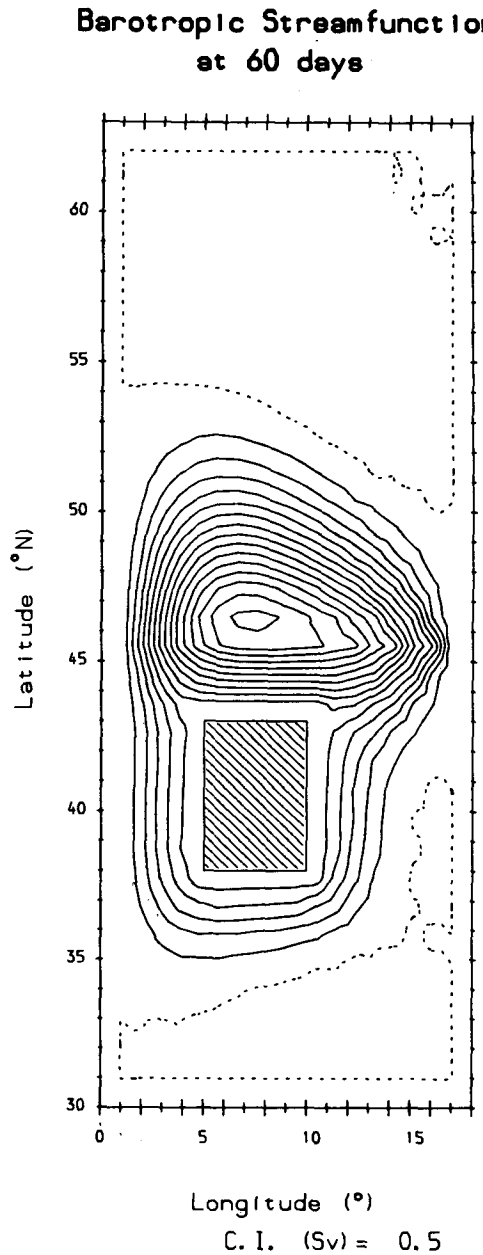

FIG. 18. Barotropic streamfunction at 60 days for the model with $\Gamma = 2.42$, incorporating an island on the ridge denoted by the hatched region.

North of the ridge, the transport is typically ⩽5% greater, except by the northern ridge face where it is up to 20% larger. There is no significant difference in transport on the ridge. By 120 days, both models develop a weak indirect circulation below the depth of the ridge, resulting from the increased importance of the second baroclinic mode. The difference in transports south of the ridge has reduced to ⩽50% at and below the top of the ridge, and above the ridge that of the no-island model is up to 5% larger.

5. Discussion

Insight into how the oceans adjust to equilibrium under some driving force is often gained by studying how the system *tends* to adjust to equilibrium under gravity in the absence of the driving forces. In the present study, the initial adjustment between two basins resulting from the formation of a pool of dense water in one is investigated. In addition to using a multilevel general circulation model, the processes are studied in an equivalent form using a two-layer model to help illustrate the interaction between stratification and topography, and the differences that arise from increased vertical degrees of freedom.

There are two aspects to the adjustment. First, it illustrates how topographic barriers contribute to basin-scale mixing and hence a reduction in stratification. Suppose deep convection leads to the formation of a pool of dense water in the interior of a basin; eventually with the help of diffusive effects the edges will intersect a coastline. The alongshore gradient in the pressure field will propagate rapidly along the coast toward the barrier as a coastally trapped Kelvin wave packet with an associated upwelling. The interaction of the offshore density gradient with the alongshore topographic gradient generates barotropic vorticity, which is transported across the basin very rapidly by double Kelvin waves, thus, setting up a basinwide anticyclonic gyre centered on the ridge edge. The magnitude of the gyre is such as to reduce the lower-layer flow onto the ridge to zero in the two-layer model, and to reduce the depth-averaged flow over the depth of the ridge to zero in the continuously stratified model. In the latter model, a further baroclinic adjustment along the face of the ridge occurs, in order to satisfy the no normal flow boundary condition. It has the form of a Kelvin-type wave producing upwelling over the depth of the ridge. The propagation is very slow, being dependent on the background stratification at depth. Closure of the anticyclonic gyre in a narrow viscous boundary layer induces upwelling at the ridge edge. The resulting alongshore pressure gradient will propagate rapidly up the coast in the same basin as coastally trapped Kelvin waves with an associated upwelling. These processes will enhance viscous and diffusive effects to produce dense, weakly stratified water below the depth of the barrier. Above the height of the barrier, the fluid will remain stratified, as the dynamics will be such as to try to impose the second basin's density field along the opposite coast.

The second aspect of the adjustment illustrates mechanisms that lead to formation of a density front on the ridge and to some extent enhancement of the stratification in the other basin due to the sinking to some depth of dense water as it flows off the barrier. It does this by showing the tendency, induced by the propagation of a relatively cold coastally trapped anomaly off the ridge, to impose the temperature (or density) on the ridge top down the face of the ridge. It is worth noting that experiments similar to the dam-break one reported by Hsieh and Gill (1986), where there is denser water on the ridge initially, were carried out and yielded similar results to the ones described for the initial adjustment. Barotropic vorticity is generated as the coastally trapped Kelvin wave packet crosses off the barrier. At this edge, double Kelvin waves propagate into the coast and thus the vorticity becomes trapped against the coast. In the two-layer model, the interfacial height perturbation propagates off the ridge almost unaffected over the outer arm of the cyclonic gyre, and the lower-layer flow is approximately zero over this region. The intense lower-layer flow off the barrier between the gyre center and the coast produces divergence and the formation of a sharp front in interfacial height, with a reduced amplitude propagating along the coast in the other basin. In the multilevel GCM, the magnitude of the cyclonic gyre is not sufficient to reduce the flow off the ridge to zero in the outer part of the boundary layer, leading to a broader but less penetrative region of downwelling. Perturbations to the velocity and density fields below the ridge top are generated at the ridge face through vertical viscous and diffusive effects, and arise farther along the coast as a result of the dispersion of the differing vertical mode coastally trapped Kelvin waves making up the signal propagating off the ridge. The form and extent of the circulation generated below the ridge top is of interest, since it is an indication of processes that would affect deep water spilling off the ridge.

Although the study was designed to look at the large-scale circulation so that the finer details of the dynamical processes occurring at the intersections of the ridge edges with the coastlines are not well resolved, the interactions at each intersection are of interest as they could occur anywhere in the world oceans where there are alongshore variations in coastal topography.

The study also highlights features of the Bryan–Cox-type numerical general circulation model, which may need to be given further consideration if it is to be used successfully in climate studies, where modeling the passage of deep water around the ocean basins is of importance. The feature most demanding of further consideration is the representation of topography by stacks of boxes. How would the adjustment process described in this study differ if a smoother representation of topography in which bottom slopes were taken into account explicitly, were adopted? To some extent this could be answered using the two-layer model: specifically, to identify the modifications resulting from the competing effects of the planetary vorticity gradient versus the topographic gradient in the barotropic vorticity balance. As pointed out in the expressions (4.1)–(4.2), the GCM tends to behave like an f-plane model unless the box depths are smaller than some critical value. Further investigation of the processes involved in the narrow boundary layer, over which flow off the ridge occurs, is also merited. Flow through the Denmark Straits, for example, is thought

to be hydraulically controlled; see, e.g., Whitehead et al. (1974). Whether it is possible to achieve flows for which inertial effects dominate viscous and diffusive effects in this boundary layer in a GCM has yet to be established. Also, the GCM considered in this study did not contain any explicit bottom boundary-layer dynamics or parameterization of entrainment processes other than $\kappa_H T_{zz}$, $\kappa_M u_{zz}$ in the heat and momentum equations, respectively. Inclusion of more sophisticated parameterizations is probably not warranted with the present formulation of topography. If this were modified to include some specification of slope, then consideration of parameterizations of turbulent entrainment and bottom friction would be worthwhile; cf. Smith (1975). The presence of an island/seamount breaking up the ridge modified the initial adjustment process by steering the barotropic flow across the ridge. It resulted in the suppression of the formation of the cyclonic gyre and a reduction in downwelling off the ridge by the coast for several months. Gullies and smaller topographic features (with length scale less than 100 km) are not well resolved, if at all, in present GCMs used for climate modeling. The above emphasizes the importance of modeling the correct connectivity between basins, i.e., the significant topographic steering features.

Acknowledgments. The author was funded by the U.K. Natural Environment Research Council and a junior research fellowship from Wolfson College, Oxford, during the course of this research. She would like to thank Drs. R. Hide and M. K. Davey for their support and encouragement, and two anonymous reviewers, who made several helpful comments on presentation.

APPENDIX

The Double Kelvin Wave in a Two-Layer Fluid

1. Step discontinuity

In a two-layer ocean with a rigid lid, waves trapped about a discontinuity in depth and which propagate with the shallower water on the rhs ($f > 0$) are found to exist. Their properties are detailed in Rhines (1977) in the context of quasi-geostrophic theory and Willmott (1984) for a finite step. For the system of equations (2.1)–(2.3), assuming a discontinuity in depth at $y = 0$ for convenience, they have the following structure

$$\psi = \exp\{i(mx - \omega t)\} \begin{cases} \psi_O \exp(-|m|y), & y \geq 0 \\ \psi_O \exp(|m|y), & y \leq 0, \end{cases}$$

and

$$h = \exp\{i(mx - \omega t)\} \begin{cases} h_O \exp(-y/b_O), & y \geq 0 \\ h_O \exp(y/b_R), & y \leq 0, \end{cases}$$

where

$$b_O = (m^2 + 1 - \omega^2)^{-1/2}, \qquad b_R = (m^2 + \gamma(1 - \omega^2)^{-1/2}, \quad \text{(A1.1)}$$

$$\omega = \left\{\frac{(\Gamma - 1)}{(\Gamma + 1)}\operatorname{sgn}(m) + \frac{(\gamma - 1)m}{(\gamma b_O^{-1} + b_R^{-1})}\right\} \times \left\{1 + \frac{(\Gamma - 1)}{(\Gamma + 1)}\frac{(\gamma - 1)|m|}{(\gamma b_O^{-1} + b_R^{-1})}\right\}^{-1}, \quad \text{(A1.2)}$$

and

$$\psi_O = \left(\frac{\Gamma^2 - 1}{4\Gamma}\right)\left\{\frac{(\Gamma - 1)}{(\Gamma + 1)} + \frac{(\gamma b_O^{-1} + b_R^{-1})}{(\gamma - 1)|m|}\right\} D_1 h_O.$$

The shallow-water double Kelvin waves are recovered in the limit $D_1/D_2 \to \infty$, and so $\Gamma \to 1$ and $\gamma \to D_{2O}/D_{2R}$. The above expressions reduce to those derived by Rhines (1977) for $\Gamma - 1 \ll 1$, (and so $\omega^2 \ll 1$). Similarly, large-scale motions ($m^2 \ll 1$) are essentially barotropic (i.e., $h_O/\psi_O \to 0$) with $\omega \to (\Gamma - 1)/(\Gamma + 1)\operatorname{sgn}(m)$, and

$$\partial\omega/\partial m \to \left(\frac{\Gamma - 1}{\Gamma + 1}\right)2\delta(m) + (1 - \gamma^{-1/2}) \times \left(1 - \left(\frac{\Gamma - 1}{\Gamma + 1}\right)^2\right)^{1/2} \quad \text{as} \quad |m| \to 0, \quad \text{(A1.3)}$$

where $\delta(m)$ is the Dirac delta function. Also, for $m^2 \gg 1$, the motion is increasingly confined to the lower layer (i.e., $u_1/u_2 \to 0$), with

$$\omega \approx \left\{\frac{(\Gamma - 1)}{(\Gamma + 1)} + \frac{(\gamma - 1)}{(\gamma + 1)}\right\} \times \left\{1 + \frac{(\Gamma - 1)}{(\Gamma + 1)}\frac{(\gamma - 1)}{(\gamma + 1)}\right\}^{-1} \operatorname{sgn}(m)$$

and $\partial\omega/\partial m \to 0$. It is noteworthy that, given usually $D_1/D_2 \leq 1$, to obtain double Kelvin waves with group velocities of order 1 requires $D_{2R}/D_1 \ll 1$.

The properties of double Kelvin waves in a two-layer ocean in which the rigid-lid approximation is not made were investigated by Bondok and Pinsent (1984). For $m^2 \ll 1$, ω becomes independent of H_1, i.e., barotropic, and tends to zero as $m \to 0$, with $\partial\omega/\partial m$ tending to $1 - \Gamma^{-1/2}$. For $m^2 \gg 1$, the frequency is dependent on H_1 and tends to $(\Gamma\gamma - 1)/(\Gamma\gamma + 1)$, with $\partial\omega/\partial m$ tending to zero.

2. Top-hat ridge

For the experiments considered in the main text, the ridge width is much greater than the Rossby radius, but of similar magnitude to the meridional extent of the long barotropic waves. Modification of the wave structure for a ridge of finite width $2W$ is as follows

$$\psi = \exp\{i(mx - \omega t)\}$$

$$\times\begin{cases}\psi_O \exp(-|m|(y-W)), & y \geqslant W\\ [\psi_O \sinh m(y+W)\\ \quad + \psi_T \sinh m(W-y)](\sinh 2mW)^{-1}, & |y| \leqslant W\\ \psi_T \exp(|m|(y+W)), & y \leqslant -W,\end{cases}$$

$$h = \exp\{i(mx-\omega t)\}$$

$$\times\begin{cases}h_O \exp(-(y-W)/b_O), & y \geqslant W,\\ [h_O \sinh(y+W)/b_R\\ \quad + h_T \sinh(W-y)/b_R]\,(\sinh 2W/b_R)^{-1}, & |y| \leqslant W,\\ h_T \exp((y+W)/b_O), & y \leqslant -W,\end{cases}$$

where b_O, b_R are given by (A1.1). The coefficients h_T, ψ_T are given in terms of h_O, ψ_O by application of the condition

$$[\psi_{yt}/D + \psi_x/D] = [(c^2/D_1)h_x],$$

at each ridge edge, where [ ] denotes the jump passing from $y = -W-$ to $-W+$, or from $y = W-$ to $W+$. Hence

$$\psi_T = \frac{\sinh 2mW}{\Gamma\omega}\{-(\Gamma-1)D_1 h_O + \{\omega(1+\Gamma\coth 2|m|W)\operatorname{sgn}(m) - (\Gamma-1)\}\psi_O\} \tag{A1.4}$$

and

$$h_T = \frac{\sinh 2mW}{\Gamma\omega}\{(\Gamma-1) + \omega(1+\Gamma\coth 2|m|W)\operatorname{sgn}(m)\}h_O + \{(\Gamma-1)^2 - \omega^2(\Gamma+1)^2 + 2\Gamma(\coth 2|m|W - 1)\} \times \frac{\psi_O}{\Gamma(\Gamma-1)D_1\cosh 2kW}. \tag{A1.5}$$

The further matching condition

$$[c^2\hat{v}] = [(c^2/D_1)\psi_x]$$

at each ridge edge gives

$$\left\{\omega\left(\frac{1}{b_O} + \frac{\coth 2W/b_R}{\gamma b_R}\right) - \left(1-\frac{1}{\gamma}\right)m\right\}h_O - \frac{\omega}{\gamma b_R \sinh 2W/b_R}h_T = \left(1-\frac{1}{\gamma}\right)(1-\omega^2)m\frac{\psi_O}{D_1} \tag{A1.6}$$

and

$$\frac{\omega}{\gamma b_R \sinh 2W/b_R}h_O - \left\{\omega\left(\frac{1}{b_O} + \frac{\coth 2W/b_R}{\gamma b_R}\right) + \left(1-\frac{1}{\gamma}\right)\right\}h_T = \left(1-\frac{1}{\gamma}\right)(1-\omega^2)m\frac{\psi_T}{D_1}. \tag{A1.7}$$

Substituting (A1.5) in (A1.6) gives ψ_O in terms of h_O, and for a nontrivial solution for $(h_O, h_T, \psi_O, \psi_T)$, the determinant of the coefficients in (A1.4)–(A1.7) must be zero, yielding a dispersion relationship for ω. Assuming $W/b_R \ll 1$, the dispersion relationship reduces to [cf. (A1.2)]

$$\omega = \pm\left\{\frac{(\Gamma-1)\operatorname{sgn}(m)}{(1+\Gamma\coth 2|m|W)} + \frac{(\gamma-1)m}{(\gamma b_O^{-1} + b_R^{-1})}\right\} \times\left\{1 + \frac{(\Gamma-1)(\gamma-1)|m|}{(1+\Gamma\coth 2|m|W)(\gamma b_O^{-1} + b_R^{-1})}\right\}^{-1}.$$

REFERENCES

Anderson, D. L. T., and R. A. Corry, 1985: Ocean response to low frequency wind forcing with application to the seasonal variation in the Florida Straits–Gulf Stream transport, *Progress in Oceanography*, Vol. 14, Pergamon, 7–40.

Bondok, S. A. W., and H. G. Pinsent, 1984: Double Kelvin waves in a two layer sea, *J. Mar. Res.*, **42**, 29–43.

Chapman, D. C., 1982: On the failure of Laplace's tidal equations to model subinertial motions at a discontinuity in depth, *Dyn. Atmos. Oceans*, **7**, 1–16.

Cox, M. D., 1984: A primitive equation, 3-dimensional model of the ocean, GFDL Ocean Group Tech. Rep. No. 1, 143 pp.

Davey, M. K., W. H. Hsieh and R. C. Wajsowicz, 1983: The free Kelvin wave with lateral and vertical viscosity, *J. Phys. Oceanogr.*, **13**, 2182–2191.

Gill, A. E., 1977: The hydraulics of rotating-channel flow, *J. Fluid Mech.*, **80**, 641–671.

——, 1982: *Atmosphere-Ocean Dynamics*, Academic Press, 662 pp.

——, M. K. Davey, E. R. Johnson and P. F. Linden, 1986: Rossby adjustment over a step, *J. Mar. Res.*, **44**, 713–738.

Hsieh, W. H., and A. E. Gill, 1986: The Rossby adjustment problem in a rotating, stratified channel, with and without topography, *J. Phys. Oceanogr.*, **14**, 424–437.

——, M. K. Davey and R. C. Wajsowicz, 1983: The free Kelvin wave in finite-difference numerical models, *J. Phys. Oceanogr.*, **13**, 1383–1397.

Johnson, E. R., 1985: Topographic waves and the evolution of coastal currents, *J. Fluid Mech.*, **160**, 499–509.

Livingstone, H. D., J. H. Swift and H. Gote Ostlund, 1985: Artificial radionuclide tracer supply to the Denmark Strait overflow between 1972 and 1981, *J. Geophys. Res.*, **90**, 6971–6982.

Longuet-Higgins, M. S., 1968: On the trapping of waves along a discontinuity of depth in a rotating ocean, *J. Fluid Mech.*, **31**, 417–434.

McCreary, J. P., 1981: A linear stratified model of the coastal undercurrent, *Phil. Trans. Roy. Soc. London*, **A302**, 385–413.

Rhines, P. B., 1977: The dynamics of unsteady currents, *The Sea*, Vol. 6, E. D. Goldberg et al., Eds., Wiley (Interscience), 189–318.

Sarmiento, J. L., 1983: A simulation of bomb tritium entry into the Atlantic Ocean, *J. Phys. Oceanogr.*, **13**, 1924–1939.

Smith, P. C., 1975: A streamtube model for bottom boundary currents in the ocean, *Deep-Sea Res.*, **22**, 853–873.

Wajsowicz, R. C., 1991: A note on the inclusion of islands and seamounts in global climate GCMs, *Ocean Modelling*, submitted.

——, and A. E. Gill, 1986: Adjustment of the ocean under buoyancy forces, part 1: The role of Kelvin waves, *J. Phys. Oceanogr.*, **16**, 2097–2114.

Whitehead, J. A., A. Leetmaa and R. A. Knox, 1974: Rotating hydraulics of strait and sill flows, *Geophys. Fluid Dyn.*, **6**, 101–125.

Willmott, A. J., 1984: Forced double Kelvin waves in a stratified ocean, *J. Mar. Res.*, **42**, 319–358.